Leopold-Franzens University of Innsbruck

# Experimental setup for trapping strontium Rydberg ions

A Thesis
submitted to the Faculty of
Mathematics, Computer Science and Physics,
in partial fulfillment of the requirements
for the degree of

MASTER OF SCIENCE

carried out at the Institute of Experimental Physics
under the guidance of assoz. Prof. Dr. Markus Thomas Hennrich,
presented by

FABIAN POKORNY

March 2014

# Kurzfassung

Rydbergatome sind Atome in hochangeregten elektronischen Zuständen. Neutrale Rydbergatome werden seit vielen Jahren in Experimenten zur Quanteninformation verwendet. Beispiele hierfür sind die bahnbrechenden Experimente von S. Haroche und H. Walther, bei denen Rydbergatome kohärent mit dem Lichtfeld von Mikrowellenresonatoren wechselwirken.
Rydbergionen sind weit weniger gut untersucht, insbesondere wurden Rydbergionen bislang noch nie gefangen. Die Arbeitsgruppe um P. Zoller hat eine interessante Methode vorgeschlagen, wie man gefangene Rydbergionen zur Quanteninformationsverarbeitung verwenden könnte. Diese Masterarbeit beschreibt einen experimentellen Aufbau, mit dem Strontiumionen gefangen und in den Rydbergzustand angeregt werden sollen.
Das Hauptaugenmerk der Arbeit liegt im Aufbau einer Ionenfalle vom Typ einer linearen Paul-Falle. Das Design der Falle wird beschrieben und die erwarteten Fallenparameter werden berechnet. Die Vakuumkammer, in welcher die Falle untergebracht ist, wird ebenso erläutert wie die aspherischen Linsen, mit welchen die gefangenen Ionen einzeln adressiert werden sollen. Das optische Auflösungsvermögen dieser Linsen wird gemessen und das Ergebnis mit simulierten Resultaten verglichen. Am Ende der Arbeit wird der Aufbau der Falle und der Vakuumkammer beschrieben.

# Abstract

For Rydberg atoms the outermost electron resides in a highly excited state. Neutral Rydberg atoms have been used in quantum information experiments since many years, in particular in the pioneering experiments by S. Haroche and H. Walther where a flying Rydberg atom interacts coherently with the photonic mode of a microwave cavity. Rydberg ions are far less investigated. In particular, trapped Rydberg ions have never been realised. The group of P. Zoller has made an interesting proposal about the use of trapped Rydberg ions for quantum information processing. In this thesis, we describe the setup of an experimental system for trapping strontium ions and exciting them to the Rydberg state.
The main focus of the thesis lies on the ion trap setup (a linear Paul trap). The design of the trap is described as well as the expected trapping parameters. The vacuum chamber which houses the trap is explained along with the aspherical lenses which will be used for individual addressing of the ions. We characterise the optical performance of these lenses and compare the results to simulations. Finally, we show in detail the assembling process of the trap and the surrounding vacuum chamber.

# Contents


**1 Introduction** **1**

**2 Trapped ions** **4**
2.1 Confining ions in electric fields . . . . . 4
2.2 Linear Paul traps . . . . . 5
2.3 Quantum computing with trapped ions . . . . . 9

**3 Trapped Rydberg ions** **12**
3.1 Properties of Rydberg atoms and ions . . . . . 12
3.2 Rydberg ions in a linear Paul trap . . . . . 14
3.3 A two-qubit phase gate with Rydberg ions . . . . . 17

**4 Experimental setup** **20**
4.1 Laser systems . . . . . 20
4.1.1 The level-scheme . . . . . 21
4.1.2 Setup of the laser systems . . . . . 22
4.2 The ion trap . . . . . 33
4.3 Vacuum chamber . . . . . 38
4.4 Addressing lens . . . . . 41
4.5 Assembly of the setup . . . . . 46
4.5.1 Cleaning and bake-out process . . . . . 46
4.5.2 Assembly of the vacuum setup . . . . . 49

**5 Summary and outlook** **54**

**A Macor oven holder** **56**

**B Custom zero-length reducer** **57**

**C NEXTorr D 100-5 vacuum pump** **58**

**Bibliography** **60**

# Chapter 1

# Introduction

Over the last few decades, information processing with computers has without doubt revolutionised not only scientific work, but also our everyday life. While the hardware used in computers relies heavily on our understanding of quantum physics (keyword semiconductors), this is not true for how computers (themselves) process information. All common devices, from the small hand-held calculator to the mightiest computer cluster processing data at some university, use algorithms that can be executed on a universal Turing machine, thus following the laws of classical physics. So, although nowadays our understanding of quantum physics is necessary to build a computer, it doesn't play a role in information processing itself.

Quantum physics describes the world to a greater extend and in much more detail than classical physics. Thus, the question whether this is also true for information processing relying on the framework of quantum physics rather than classical physics is completely justified. To find a way to compare the power of computing within different frameworks, one can look at how *efficient* a problem or algorithm can be solved by the respective system. Efficiency in the context of computer science describes how much time, resources and memory is needed to solve a problem. If these parameters scale polynomially (for example with the size of a number that should be factorised or with the amount of particles in a system), an algorithm is efficient, for superpolynomial or exponential scaling it is inefficient. Thus a system that can solve a set of problems efficiently which another system can only solve inefficiently is more powerful regarding these tasks than the latter.

Computer scientists and physicists were already thinking about this topic for quite some time when in 1982 Richard Feynman investigated the problem of efficiently simulating a quantum system on a classical computer [1]. He concluded that this task is not possible and suggested to use a quantum system to simulate another quantum system, thus proposing the use of a quantum computer. Only three years later, in 1985, David Deutsch introduced the quantum Turing machine and showed that a quantum computer is capable of performing arbitrary computations [2]. With these two proposals it was clear that a quantum computer could be used to solve certain problems more efficiently than a classical system. However, neither Feynman nor Deutsch suggested what kind of

quantum system could be used to realise such a computer. Thus quantum computation was more a theoretical than an experimental field of physics, a circumstance that was not changed by Peter Shore's invention of his famous algorithm for finding the prime factors of any given number in 1994 [3]. However, this proposal showed that having a quantum computer would be a nice and useful thing, especially since it would render important parts of nowadays encryptions methods useless. With this particular motivation the search for realistic physical systems that could act as quantum processors was intensified. Shortly afterwards, in 1995, the first suggestion for an experimental scheme that could be used for quantum computation was introduced by Ignacio Cirac and Peter Zoller. They proposed a system of trapped and cooled ions for realising the required quantum operations [4]. One of the key components of the experimental scheme, a controlled bit flip of a single ion, was realised not even a year later at the National Institute of Standards and Technology in Boulder by the group of David Wineland [5], thus marking the start of experimental quantum computation. Although nowadays researchers additionally study the use of other systems like optical photons, cavities and electrical and nuclear spins [6], the trapped ions approach is still one of the most advanced fields [7, 8] and experimental research groups all over the world investigate various aspects of quantum computation and quantum information using trapped ions [9].

Building a system suitable for quantum computation is a difficult and demanding task. Since any uncontrolled disturbance of the physical qubits results in decoherence and thus in erroneous calculations, seemingly contradicting physical properties are required. On one hand the system needs to be very well isolated from the surrounding environment in order to prevent decoherence and enable long livetimes of the quantum states. On the other hand, control with tremendous precision is essential to successfully manipulate the system. Thus, one needs an interaction channel between qubit and environment which can be switched on and off depending on the experiment's requirements. David DiVincenzo summarised the general physical criteria which a system suitable for quantum information processing hast to meet [10]:

1. A scalable physical system with well characterised qubits.
2. The ability to initialise the state of the qubits as a simple fiducial state.
3. Long relevant decoherence times, much longer than the gate operation time.
4. A universal set of quantum gates[1].
5. A qubit-specific measurement capability.

While the first fife criteria are necessary for quantum computation and quantum simulation, building a quantum network requires two additional ones:

6. The ability to interconvert stationary and flying qubits.
7. The ability to faithfully transmit flying qubits between specified locations.

[1] In the most simple case single-qubit and entangling two-qubit gates.

Nearly two decades have passed since the proposal by Cirac and Zoller and huge progress has been made in the field of ion trap quantum computers. A good summary of the resent developments can be found in [7] and [9]. One issue that emerged as a major challenge for quantum computation with trapped ions (but also for quantum computation in general) is the requirement of a scalable system. In ion trap quantum computation, an increasing number of ions in the trap is accompanied by an increasing complexity of the common vibrational mode spectrum which represents the phonon data bus. This makes it increasingly difficult to exchange information between the ion qubits in a larger crystal (see section 2.3 for more details). To counter this problem, the group of Peter Zoller proposed a new approach for trapped ion quantum computation in 2008 [11]. Exciting the trapped ions into the Rydberg state allows interactions between the ions that are independent of the motional modes[2] and thus are not restricted by these limitations.

The following thesis is based upon an experimental setup to realise this new approach. The final aim of out experiment is to realise quantum computation with trapped Rydberg ions. The thesis is divided in two main parts: chapter two and three introduce the reader to the theoretical background of the experiment. Firstly, the method of ion trapping is explained with focus on the linear Paul trap. Secondly, the properties of Rydberg atoms and ions are described along with their use for quantum computation. The second and main part of the thesis describes the setup of the experiment. We have built the setup now for around one and a half years and a detailed description of the different parts that are set up so far is given (with focus on my Master project). Here, the laser system is introduced in section 4.1 along with the level scheme of strontium to illustrate the different tasks of each laser wavelength we use. Then, section 4.2 describes the linear Paul trap, its architecture and trapping parameters. Next, section 4.3 explains is the vacuum chamber which houses the trap followed by section 4.4 about the lenses used for addressing and imaging individual ions. Measured values of the imaging resolution are compared to simulations in order to evaluate the imaging capabilities of the system. The final section 4.5 of this chapter explains the assembly of the ion trap and the vacuum chamber. The cleaning and bake-out procedure is presented in detail, afterwards the assembly of the trap and the vacuum chamber are explained. The thesis ends with a summary on the status of the experiment and an outline of the next steps towards trapped Rydberg ions.

[2] At least to first order.

# Chapter 2

# Trapped ions

Ion traps are used in many different fields of physics, including quantum computation. There are several types of ion traps which rely on different methods to achieve spatial confinement. Paul traps, for example, use oscillating electric fields for confinement, while Penning traps use a combination of static electric and magnetic fields. Since our experiment will use a linear Paul trap, this chapter focuses on this type of trap. Important trap parameters such as the stability parameter and the radial and axial frequencies are derived and discussed.

## 2.1 Confining ions in electric fields

An electric field acting on a charged particle gives rise to forces that are much larger[1] than the forces experienced by a neutral atom in a magnetic field [12]. Comparing the forces acting on an ion and a neutral atom in the respective field, one gets

$$F_{\text{ion}} = eE \tag{2.1}$$

and

$$F_{\text{atom}} = \mu_B \left| \frac{dB}{dz} \right| \quad , \tag{2.2}$$

where $e$ is the charge of the particle, $E$ the electric field, $\mu_B$ the Bohr magneton and $dB/dz$ the magnetic field gradient. A singly-charged particle in a typical ion trap (with an electrode separation of $5\,\text{mm}$ and an applied voltage of $500\,\text{V}$) experiences a force $F_{\text{ion}} \approx 10^{-14}\,\text{N}$. In comparison, a neutral atom with a magnetic moment of one Bohr magneton in a magnetic field with a gradient of $dB/dz = 10\,\text{T m}^{-1}$ (which is a typical value for a magnetic trap) only experiences a force $F_{\text{atom}} \approx 10^{-22}\,\text{N}$. We see that using electric fields to confine charged particles leads to trapping potentials that are much deeper than the trapping potentials achieved for atoms with magnetic or magneto-optical

[1] At least for typical field values used for trapping atoms and ions.

traps[2]. Trapping potentials of ion traps are easily deep enough to confine ions at room-temperature and above. There is, however, one difficulty that must be overcome in order to achieve a trapping potential with electric fields, namely Earnshaw's theorem. Earnshaw's theorem, proven by Samuel Earnshaw in 1842, states that *a charge acted on by electrostatic forces cannot rest in stable equilibrium in an electric field* [12]. This means that it is not possible to confine charged particles using purely static electric fields. Earnshaw's theorem follows directly from the Maxwell equations. The equation for the divergence of an electric field in a region with no free charge density has the same structure as the Laplace equation

$$\nabla \cdot \vec{E} = \Delta\varphi = 0 \quad , \tag{2.3}$$

which means that there are no sources or sinks in this area and so there is no potential maximum or minimum. This can easily be shown by assuming the following harmonic potential

$$\varphi = ax^2 + by^2 + cz^2 \quad . \tag{2.4}$$

For this potential to be confining all three parameters $a, b$ and $c$ must be larger than zero. Applying equation 2.3 to this potential however leads to

$$a + b + c = 0 \quad . \tag{2.5}$$

This equation cannot be fulfilled for the condition $a, b, c > 0$, which means that at least in one direction the potential is not confining. To trap ions, one must circumvent Earnshaw's theorem. There are two main methods to do so: either one uses a combination of perpendicular static electric and magnetic fields or one works with dynamic electric fields. The former method is used for Penning traps, the latter for Paul traps. Since we will be working with a linear Paul trap, the focus of the next section lies on the trapping of ions with dynamic electric fields.

## 2.2 Linear Paul traps

Paul traps use dynamic electric fields to confine charged particles. There is an easy to understand mechanical analogue for the resulting trapping potential which is shown in figure 2.1: a ball moving on a rotating, saddle-shaped surface. Why this setup is confining the ball can easily be seen: leaving the saddle at rest, the ball will move in the direction of the downwards curved sides. If the surface starts to rotate, the ball follows the changing direction of the "valley". Due to its inertial mass, the ball does not follow the change in direction immediately. At the right rotation frequency, the ball will always follow the valley without moving further down and is thus confined. This picture of a "changing potential" does not perfectly describe the dynamics of the electric fields in a Paul trap since the electric potential is not rotating. Its changes are better described as a waving, the "hillside" flanks becoming valleys and then changing back (and vice versa).

[2]Typical values for the trapping depth of a ion trap lie in the range of several hundred eV which means that particles with energies corresponding to temperatures up to several $10^6$ K can be trapped. In contrast, the trapping depth of a magnetic trap lies in the range of mK.

However, the result for the charged particle is the same. The following paragraphs discuss how such a potential can be achieved with electric fields. For an overview on this topic see [12]. A deeper discussion can be found in [13–15].

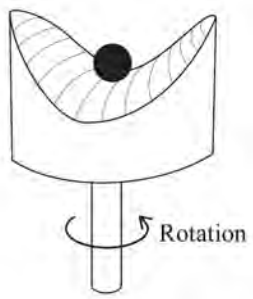


**Figure 2.1:** A ball moving on a rotating saddle-shaped surface may be stably confined [12].

In a linear Paul trap the confining potential is generated by four electrodes which are parallel to the trapping axis (usually labelled as the z-axis), see figure 2.2. This configuration leads to a two-dimensional radial quadrupole potential of the form

$$\Phi\left(x,y,z,t\right)=\frac{U_{\text{rf}}}{2r_0^2}\cos\left(\Omega_{\text{rf}}t\right)\left(x^2-y^2\right) \quad , \tag{2.6}$$

where $U_{\text{rf}}$ is the magnitude of the rf-potential between opposing electrodes, $\Omega_{\text{rf}}$ is the frequency of the rf-potential and $r_0$ is the minimum distance between the trapping axis and the electrodes.

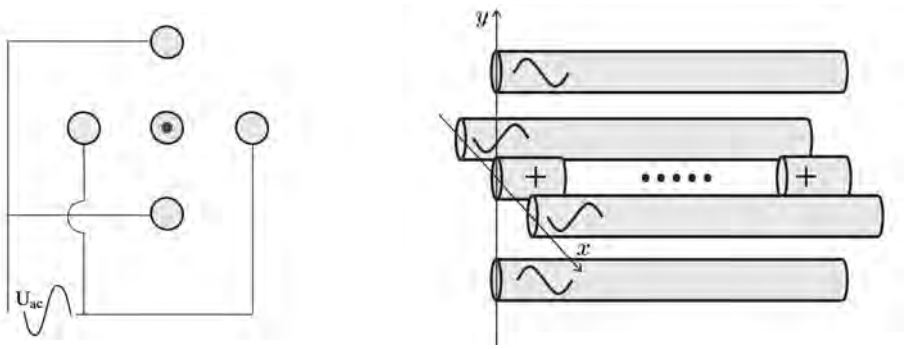


(a) (b)

**Figure 2.2:** Schematics of a linear Paul trap with endcap electrodes for axial confinement. Figure (a) shows the trap in the x-y-plane. The four rods are connected pairwise to the diagonally opposite one and thus form a quadrupole field. In (b) one can see the position of ions in the trap and the endcap electrodes which cause confinement along the z-axis [12].

This potential alone is not confining in all three dimensions, the ions can move along the z-axis. Confinement along the z-direction is achieved by applying an additional static electric potential $U_{\text{cap}}$ to two electrodes that are aligned with this axis, see

figure 2.2 (b). The potential is chosen such that the charged particles are repelled by the electrodes and thus confined in all three dimensions.

To investigate the behaviour of a charged particle in a potential of the form given in equation 2.6, we look at the equation of motion which can be derived for the motion along the x-axis

$$F = m\ddot{x} = eE = -e\frac{d\Phi}{dx} \quad . \tag{2.7}$$

Thus

$$m\ddot{x} = -e\frac{d\Phi}{dx} \tag{2.8}$$

$$= -\frac{eU_{\text{rf}}}{r_0^2}\cos\left(\Omega_{\text{rf}}t\right)x \quad . \tag{2.9}$$

Substituting $\tau = \Omega_{\text{rf}}t/2$ leads to

$$\frac{d^2x}{d\tau^2} = -\frac{4eU_{\text{rf}}}{\Omega_{\text{rf}}^2 m r_0^2}\cos\left(2\tau\right)x \quad . \tag{2.10}$$

This result has the form of the simplified Mathieu equation

$$\frac{d^2x}{d\tau^2} + \left(a_x - 2q_x\cos\left(2\tau\right)\right)x = 0 \quad , \tag{2.11}$$

where $a_x$ is zero since we have not included any DC voltage in equation 2.6. This omission is of course not correct since we apply a DC voltage to the endcap electrodes for confinement along the z-axis. However, the offset $a_x$ is not dependent on the $U_{\text{rf}}$ field. Thus, the equation of motion and the resulting Mathieu equation is the same in the y-direction as in the x-direction (up to an additional minus sign) so that the resulting equations of motion in all three dimensions are

$$\frac{d^2x}{d\tau^2} + \left(a - 2q\cos\left(2\tau\right)\right)x = 0 \tag{2.12}$$

$$\frac{d^2y}{d\tau^2} + \left(a + 2q\cos\left(2\tau\right)\right)y = 0 \tag{2.13}$$

$$\frac{d^2z}{d\tau^2} + 2az = 0 \quad , \tag{2.14}$$

with

$$\tau = \frac{\Omega_{\text{rf}}t}{2}, \qquad a = \frac{4\left|e\right|\alpha U_{\text{cap}}}{mZ_0^2\Omega_{\text{rf}}^2}, \qquad q = \frac{2\left|e\right|U_{\text{rf}}}{mr_0^2\Omega_{\text{rf}}^2} \quad . \tag{2.15}$$

Equation 2.14 describes the motion of the trapped particle along the z-axis and has no time-dependent term since the field in the z-direction is static. The stability parameter $a$ depends on the voltage applied to the endcap electrodes while the stability parameter $q$ depends on the rf-voltage. The *geometry factor* $\alpha$ is a numerical factor which depends on the trap geometry. For our trap we expect this parameter to be $\alpha \approx 0.042$, a value that is similar to that of other linear traps[3]. $z_0$ is half the distance between the two endcap electrodes and $m$ is the mass of the confined ion. Parameters $a$ and $q$ define the regions where stable trapping is possible. Because the distance $L = 2z_0$ between the endcap electrodes is usually much larger than the distance $r_0$ between the blade electrodes and the trapping axis, one may assume that the trap is operated with $a \approx 0$. In this case, stable trapping is possible within a range of $0 < q < 0.9$. Figure 2.3 shows the general stability conditions for an ideal linear Paul trap.

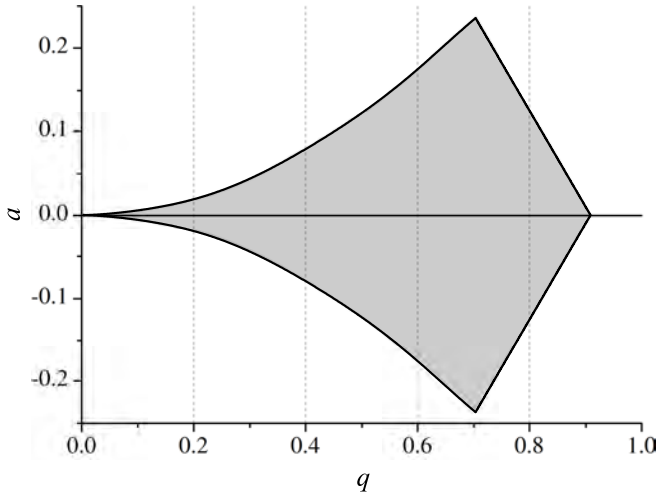


**Figure 2.3:** The lowest stability domain for the ideal linear Paul trap. A stable trapping potential is provided if the parameters $a$ and $q$ are kept within the shaded region [17].

For $a, q \ll 1$, stable solutions to equations 2.12 and 2.13 are

$$x(\tau) = x_0 \cos(\omega_x \tau + \varphi_x) \left(1 + \frac{q}{2} \cos 2\tau\right) \tag{2.16}$$

and

$$y(\tau) = y_0 \cos(\omega_y \tau + \varphi_y) \left(1 + \frac{q}{2} \cos 2\tau\right) \tag{2.17}$$

respectively, with initial phases $\varphi_x$ and $\varphi_y$. Since $\tau = \Omega_{\text{rf}} t/2$, the frequencies $\omega_x$ and $\omega_y$ take the form

$$\omega_x = \frac{\Omega_{\text{rf}}}{2} \sqrt{\frac{q^2}{2} + a} \qquad \text{and} \qquad \omega_y = \frac{\Omega_{\text{rf}}}{2} \sqrt{\frac{q^2}{2} - a} \quad . \tag{2.18}$$

[3]For example, the linear Paul trap in the $^{40}$Ca experiment here in Innsbruck has a stability parameter of $\alpha \approx 0.075$ [16].

If we again assume that the trap is operated with $a \approx 0$, we see that the radial frequency is the same along the x- and the y-axis, thus leading to

$$\omega_{\text{rad}} = \omega_x = \omega_y = \frac{q\Omega_{\text{rf}}}{2\sqrt{2}} = \frac{|e|\, U_{\text{rf}}}{\sqrt{2}\Omega_{\text{rf}} m r_0^2} \quad . \tag{2.19}$$

In the same way the axial frequency can be derived from equation 2.14 to

$$\omega_{\text{ax}} = \sqrt{\frac{2\,|e|\,\alpha U_{\text{cap}}}{m z_0^2}} \quad . \tag{2.20}$$

It is interesting to see what happens to the trapping frequencies when $a$ cannot be assumed to be zero. Comparing $a$ to the axial frequency $\omega_{\text{ax}}$ gives

$$a = \frac{2}{\Omega_{\text{rf}}^2}\omega_{\text{ax}}^2 \quad . \tag{2.21}$$

Inserting this result into 2.18 leads to

$$\omega_{x/y} = \frac{\Omega_{\text{rf}}}{2}\sqrt{\frac{q^2}{2} \pm \frac{2}{\Omega_{\text{rf}}^2}\omega_{\text{ax}}^2} \tag{2.22}$$

$$= \sqrt{\omega_{\text{rad}}^2 \pm \frac{\omega_{\text{ax}}^2}{2}} \quad . \tag{2.23}$$

We see that the radial frequency is neither completely independent from the axial frequency nor from the voltage applied to the endcap electrodes. It is noteworthy that increasing $U_{\text{cap}}$ decreases the radial confinement. If the trap is operated in a regime where $\omega_{\text{ax}} \ll \omega_{\text{rad}}$ is not valid, the trapping potential is not linear. We now have all the formulations we need to estimate the performance and trapping parameters for our linear ion trap. See chapter 4.2 for the setup of the trap and its parameters.

## 2.3 Quantum computing with trapped ions

There are different approaches to realise a quantum computer. Beside trapped ions, researchers work with systems like photons, cavities, superconducting devices, quantum dots, neutral atoms, and electronic and nuclear spins [6]. Amongst these physical systems the use of trapped ions is one of the most advanced [8].

The idea to use cold trapped ions for quantum computation was first introduced by Ignacio Cirac and Peter Zoller in 1995 [4] and huge advances have been made in this field of research since then [7]. A short outline of the historic development of quantum computation and its general principles was already given in the introduction of the thesis, so this section focuses on quantum computation with ions, its advantages but also certain limitations concerning scalability.

One of the most important properties of a system suitable for quantum computation is a controlled interaction with the surrounding environment. The system has to be very well isolated to allow for long coherence times for the qubits, yet it must also offer the possibility to prepare, control, and measure the qubit state very precisely. So there has to be an interaction which can be switched on and off fast and with high precision. Trapped ions can be very well isolated from the environment. The trap is housed in an ultra-high vacuum (UHV) environment so there is very little interaction between the trapped ion qubits and background atoms. Also, electrical trapping fields can be controlled with precise electronics such that they do not disturb the ions, for example due to sudden frequency or amplitude shifts. External stray fields can shift the electronic state of the qubit, thus it is important to eliminate stray field sources or shield the setup if elimination is not possible in the first place.

Laser light is used in most ion trapping experiments to precisely control the interaction between ions and environment. The spatial separation of a few micrometers between neighbouring ions due to Coulomb repulsion allows for individual addressing of ions with a focused laser beam. Nowadays, trapped ion crystals which are laser-cooled provide one of the most precisely controllable quantum systems available in laboratories [7]. In quantum computation experiments with trapped ions the qubits are usually represented by internal electronic states of the trapped ions and the qubit state is either manipulated by lasers or microwave fields. Quantum information is processed by transferring quantum information to the collective quantised motion of the trapped ions. Here the common vibrational modes of a linear ion chain form a phonon data bus which is used to perform operations between ion qubits (Cirac and Zoller) or to mediate an interaction that leads to collective qubit flips (Mølmer and Sørensen [18]). The strong repulsion between the ions results from the strong Coulomb interaction between them. However, the spectrum of these collective motional modes is strongly dependent on the number of ions in the chain. The higher is number (and thus the higher the mass of the chain), the lower is the distance between the different motional modes, which causes the spectrum to become increasingly complex. One approach to circumvent this issue is to use a different interaction mechanism like the Rydberg interaction for quantum information processing (like we want to do in our experiment). Another approach is to split a large ion crystal into smaller sub-units and to shuttle ions between these traps to exchange the quantum information [19].

The field of quantum computation with trapped ions developed rapidly after Cirac and Zoller proposed their idea (the first result was published not even a year later by the group around David Wineland at NIST [5]). The reason for this fast development was that ion traps were already in use for quite some time. Several key concepts required for quantum computation had already been demonstrated, among them the initialisation and readout of internal electronic states, long coherence times, and laser cooling. All these properties make trapped ions a useful system for quantum information processing. The list below summarises how well ion trap quantum computers fulfil the DiVincenzo criteria so far [7]:

1. **A scalable physical system with well characterised qubits:** The qubit state is encoded in the internal electronic states of each ion. A linear ion crystal confined in a linear Paul trap is used as qubit register. So while the requirement of well characterised qubits is met, the scalability is not completely solved yet since the ion strings cannot be made arbitrarily long. However, there exist some promising approaches towards this problem like distributing the ions among several traps or moving away from using motional modes altogether (for example using the Rydberg interaction for entangling gates as envisioned in our experiment).

2. **The ability to initialise the state of the qubits to a simple fiducial state:** Optical pumping with laser light is a direct way to prepare ions in a well-defined electronic state. Fidelities of $0.99$ and higher can be achieved [20].

3. **Long relevant decoherence times, much longer than the gate operation time:** Coherence times of several tens of milliseconds up to a few seconds are typical values that can be achieved in current ion trap experiments. Quantum operations take place at a time scale of less than $100\,\mu$s which is more than two orders of magnitude faster than the coherence time.

4. **A universal set of quantum gates:** DiVincenzo proved in 1995 that every general quantum circuit can be realised with just single and two-qubit gates [21]. In ion traps single qubit gates can be realised by coupling the two qubit levels with laser light or performing coherent Rabi oscillations. Two-qubit gates can be implemented in different ways, examples are the beforehand mentioned Cirac-Zoller [4] or the Mølmer-Sørensen gates [18].

5. **A qubit-specific measurement capability:** One method of detecting the state of a qubit is fluorescence detection. One of the two qubit states is excited with laser light to a short-lived auxiliary level from where it decays back to the initial state and emits fluorescence photons. The second qubit state stays untouched and does not emit photons. The emitted fluorescence photons (or the lack thereof) indicate which state was occupied by the qubit. The detection error of the fluorescence detection can be $< 1 \cdot 10^{-3}$ on a photomultiplier.

The status of the additional DiVincenzo criteria for quantum networks:

6. **The ability to interconvert stationary and flying qubits:** Storing ions in high-finesse cavities can sufficiently increase the coupling between the ion and photons in the cavity mode and thus allows mapping the ions' internal state onto a photonic state. In this way the quantum information of the stationary qubit (ion) is transferred to a flying qubit (photon).

7. **The ability to faithfully transmit flying qubits between specified locations:** Photons carrying quantum information can be coupled into and sent through fibres. At the target location the conversion to a stationary qubit could be performed with an ion inside a high-finesse cavity. This was so far only realised with neutral atoms [22] but should also be possible with trapped ions.

# Chapter 3

# Trapped Rydberg ions

A Rydberg state is a quantum-mechanical state of a highly excited atom, ion or molecule with one electron close to the ionisation limit. Atoms and ions[1] with such high principal quantum numbers $n$ represent a strange overlap of the classical and the quantum world and feature extraordinary properties. In this chapter we will first summarise these special features of Rydberg atoms regarding their dependence on $n$ and, since we experiment with Rydberg ions, the charge $Z$ of the ionic parent core. In the second section of this chapter we will discuss how Rydberg ions behave in an ion trap. Finally, in the third section we will give an example of how trapped Rydberg ions can be used to realise a two-qubit phase gate.

## 3.1 Properties of Rydberg atoms and ions

The high principal quantum number $n$ of Rydberg atoms leads to number of extraordinary physical features compared to atoms in lower excited states or the ground state [23, 24]. The high excitation of one electron leads to a very small ionisation energy, the potential for large orbital angular moments and high polarisability. Due to the large distance between the excited electron and the ionic parent core, their interaction is very well described by pure Coulomb interaction. Thus, the overall structure and basic properties of such atoms and ions are very similar to those of the hydrogen atom. The following paragraphs discuss the dependency of physical properties of Rydberg atoms from the principal quantum number $n$ and the charge $Z$ of the ionic parent core. For a neutral atom this value is $Z = 1$ while in our experiment the singly-charged strontium ions will have a core charge of $Z = 2$.

The **characteristic radius $r_n$** and the **geometric area $S_n$** of Rydberg atoms are strongly dependent on the values of $n$. The properties grow with

$$r_n \approx \frac{n^2 a_0}{Z} \tag{3.1}$$

[1]Throughout the chapter the phrase "Rydberg atoms" also includes Rydberg ions unless stated otherwise.

and

$$S_n \approx \frac{\pi {a_0}^2 n^4}{Z^2} \quad , \tag{3.2}$$

where $a_0 = 4\pi\epsilon_0\hbar^2/me^2 = 5.29 \cdot 10^{-11}$ m is the Bohr radius, $\hbar$ is the reduced Planck constant and $e$ and $m$ are the electrons charge and mass, respectively. Please note that for both the radius $r_n$ as well as the geometric area $S_n$ the dependence on $n$ is stronger than it is on $Z$. It is also interesting to see how fast the radius $r_n$ of Rydberg atoms grows with $n \gg 1$. For $n \approx 100$ Rydberg atoms already have macroscopic sizes in the range of half a micrometer and thus are around $10^4$ times larger than typical atoms in the ground state (but still smaller than the average distance of around $5\,\mu$m between ions in a linear Paul trap). In comparison with neutral Rydberg atoms, a singly-charged Rydberg ion has about half the radius $r_n$ and quarter of its geometric area $S_n$.

The **energy spectrum $E_n$** and the **radiative properties** of hydrogen atoms and hydrogen-like ions share many of their basic energy and spectral characteristics like ionisation energy or transition wavelengths between neighbouring states. The electronic energy can be derived from the nonrelativistic Schrödinger equation with the Coulomb interaction $U(r) = -Ze^2/r$ and has the form

$$E_n = \frac{-Z^2 Ry}{n^2} \quad , \tag{3.3}$$

where $Ry = 13.606$ eV is the Rydberg constant. Note that the power of $n$ and $Z$ in equation 3.3 is the same. The line spectrum given by transitions from Rydberg states to the respective multi-electron ground state corresponds to the wavelength regime of visible and near ultra-violet light for Rydberg atoms. The photon energy increases drastically for Rydberg ions, reaching from the UV regime for singly-charged ions to the X-ray regime for multicharged ions. The transition frequencies between two neighbouring energy levels with the principal quantum number $n$ and $n \pm 1$ can be written as

$$\omega_{n,n\pm1} \approx \frac{2Z^2 Ry}{\hbar n^3} \quad . \tag{3.4}$$

The wavelength corresponding to these frequency is given by

$$\lambda_{n,n\pm1} = \frac{2\pi c}{\omega_{n,n\pm1}} \quad , \tag{3.5}$$

where $c$ is the speed of light. The transition wavelength thus increases with the principal quantum number[2] as $n^3$, leading to wavelengths in the micron-regime for $n \sim 10$ and centimetres for $n \sim 100$. The radiation lifetime of a Rydberg state (taking spin-orbit interactions into account) has the form

$$\tau_n \approx \frac{n^5}{3A_0 Z^4 \ln(n/1.1)} \quad , \tag{3.6}$$

[2]In radioastronomy researchers observed signals from Rydberg atoms with $n \sim 300$ and higher which corresponds to wavelengths in the meter regime.

where $A_0$ is the Einstein coefficient

$$A_0 = \frac{8\alpha^3 (v_0/a_0)}{3\pi\sqrt{3}} = 7.9 \cdot 10^9 \frac{1}{\mathrm{s}} \quad ,$$

$\alpha = 1/137$ is the fine structure constant and $v_0 = \alpha \cdot c = 2.19 \cdot 10^6$ m/s the atomic unit of velocity. $a_0$ is again the Bohr radius. Please note that equation 3.6 arises from an averaging over the $lm$-sublevels of the highly excited state. Due to this averaging the relation of $\tau_n \propto n^5$ is only correct for states with large orbital angular momentum ($l \sim n$), for cases with small orbital angular momentum ($l \ll n$) the proportionality changes to $\tau_n \propto n^3$. Latter behaviour is more important for our experiment since it is easier to access the low angular momentum states (s and d) via two-photon laser excitation starting from a d-state. Nevertheless, for both cases the $\tau_n$ increases fast with increasing values of $n$. For example, states with a principal quantum number in the regime of $n \gg 100$ have radiation lifetimes larger than 10 s. The following table 3.1 summarises the dependence of the physical values from $n$ and $Z$ and compares the numerical values for Rydberg states of atoms and ions.

| Physical parameters | | | Rydberg atom ($Z = 1$) | | Rydberg ion ($Z = 2$) | |
|---|---|---|---|---|---|---|
| Property | Expression | Unit | $n = 10$ | $n = 100$ | $n = 10$ | $n = 100$ |
| $r_n$ | $\frac{a_0 n^2}{Z}$ | m | $5.3 \cdot 10^{-9}$ | $5.3 \cdot 10^{-7}$ | $2.65 \cdot 10^{-9}$ | $2.65 \cdot 10^{-7}$ |
| $\omega_{n,n\pm1}$ | $2\frac{Z^2 Ry}{\hbar n^3}$ | Hz | $4.1 \cdot 10^{13}$ | $4.1 \cdot 10^{10}$ | $1.7 \cdot 10^{14}$ | $1.7 \cdot 10^{11}$ |
| $\lambda_{n,n\pm1}$ | $\frac{2\pi c}{\omega_{n,n\pm1}}$ | m | $4.6 \cdot 10^{-5}$ | $4.6 \cdot 10^{-2}$ | $1.1 \cdot 10^{-5}$ | $1.1 \cdot 10^{-2}$ |
| $\tau_n$ | $\frac{n^5}{3A_0 Z^4 \ln(n/1.1)}$ | s | $8.4 \cdot 10^{-5}$ | 17 | $5.3 \cdot 10^{-6}$ | 1.1 |

**Table 3.1:** Physical properties of Rydberg states. The characteristic radius $r_n$, the transition frequency $\omega_{n,n\pm1}$, the transition wavelength $\lambda_{n,n\pm1}$, and the radiation lifetime $\tau_n$ for the states with principal quantum number $n = 10$ and $n = 100$ are compared for Rydberg atoms ($Z = 1$) and single-charged Rydberg ions ($Z = 2$) [24].

## 3.2 Rydberg ions in a linear Paul trap

As already stated, Rydberg atoms and ions with high principal quantum numbers $n$ are large compared to the usual size of quantum objects. This has a severe impact on the behaviour of Rydberg ions in the electric potential of the ion trap [11, 25]. In contrast to ions with low-lying electronic states, Rydberg ions cannot be treated as a point charge but rather have to be seen as a composite object, consisting of the valence electron in the highly excited Rydberg state and the ionic parent core. In the following section we want to take a quick look at the nature of the changes caused by this difference compared to trapped ions in low lying states.

A mayor difference between ions and Rydberg ions in a linear trap is the length scale associated with the system. Particles inside the ion trap oscillate due to the external

trapping frequency. This frequency typically lies in the order of a megahertz, which corresponds to an oscillator length (extension of the wave packet in the motional ground state) of roughly $10\,\text{nm}$. This length scale is much larger than the electron orbit of an ion and thus the ion can be treated as a point-like charge oscillating in the trapping potential. However, this approximation is not true for Rydberg ions due to the large orbit of the valence electrons caused by a high $n$. It was already shown in the previous section that Rydberg ions offer characteristic radii on the order of $r_n \sim 100\,\text{nm}$ and larger and thus can easily exceed the oscillator length of the trap. However, Rydberg ions in an ion chain still can be treated as being well separated spatially since the Coulomb repulsion results in a spacing at the order of typically $5\,\mu\text{m}$ between them. This length scale is much larger than $r_n$, even for very large principal quantum numbers (this dimension is only realised for $n > 300$ which might not be stable in the trap anymore). Thus the electron orbits of adjacent Rydberg ions do not overlap. Figure 3.1 shows the described situation in detail.

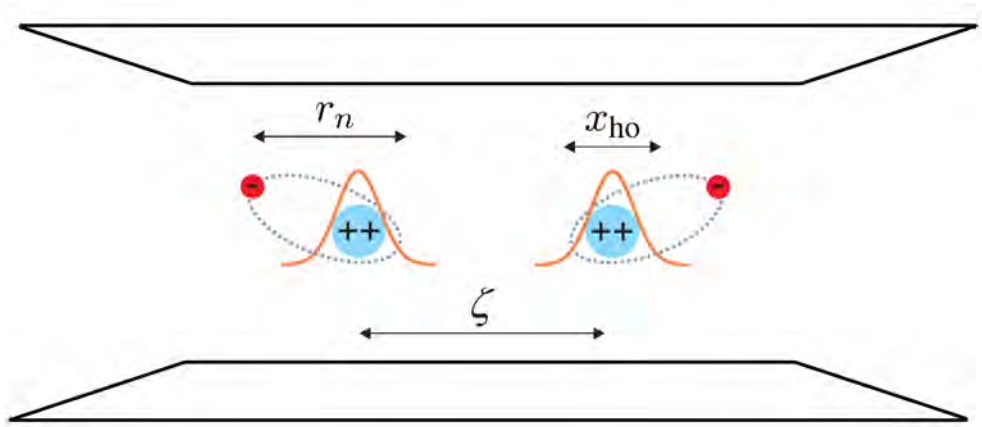


**Figure 3.1:** Typical length scales of cold Rydberg ions in a linear Paul trap (the dimensions are not to scale). The external trapping frequency is typically in the order of several MHz, resulting in an oscillator length $x_{\text{ho}}$ of approximately $10\,\text{nm}$. So while the orbit $r_n$ of the Rydberg electron is on the order of $100\,\text{nm}$ and thus much larger than $x_{\text{ho}}$, the Rydberg ions are separated by a typical spacing of $\zeta \approx 5\,\mu\text{m}$, resulting in the length scale $x_{\text{ho}} < r_n \ll \zeta$. Trapped Rydberg ions hence have to be treated as composite objects with an internal structure [11].

This difference of length scales between ions and Rydberg ions results in a different treatment of their behaviour inside the trap. Rydberg ions must be understood as a compound object, consisting of the highly excited electron and the double-charged ionic parent core. This electron is bound to the core through the Coulomb force and both electron and core move in the electric field of the trapping potential. This character of the Rydberg ions gives rise to a specific coupling of the electronic and the external motion in the presence of the trapping potential. As a result, the trapping frequencies of the Rydberg ions change compared to the frequencies experienced by ions in the ground state. The following few paragraphs outline the nature of this change. The details of the calculations can be found in [11] and [25].

The quadrupole field forming the trapping potential of a standard Paul trap can be written as

$$\Phi(\mathbf{r},t) = \alpha\cos(\omega t)\left[x^2 - y^2\right] - \beta\left[x^2 + y^2 - 2z^2\right] \quad , \tag{3.7}$$

where $\omega$ is the frequency of the RF drive and the parameters $\alpha$ and $\beta$ describe the radial and axial gradients of the electric field, respectively. Both $\alpha$ and $\beta$ are determined by the geometry of the trap. The Hamiltonian of a single Rydberg ion in the electric potential of the Paul trap can be expressed as

$$H = H_{\text{CM}} + H_{\text{el}} + H_{\text{CM-el}} + H_{\text{mm}} \tag{3.8}$$

with

$$H_{\text{CM}} = \frac{\mathbf{P}^2}{2M} + \frac{1}{2}M\omega_z^2 Z^2 + \frac{1}{2}M\omega_\rho^2\left(X^2 + Y^2\right) \quad , \tag{3.9}$$

$$H_{\text{el}} = \frac{\mathbf{p}^2}{2m} + V(|\mathbf{r}|) - e\Phi(\mathbf{r},t) + H_{\text{FS}} \quad , \tag{3.10}$$

$$H_{\text{CM-el}} = -2e\left[\alpha\cos(\omega t)(Xx - Yy) - \beta(Xx + Yy - 2Zz)\right] \quad , \tag{3.11}$$

$$H_{\text{mm}} = -\frac{2e\alpha}{M\omega}\sin(\omega t)(XP_x - YP_y) - \frac{e^2\alpha^2}{M\omega^2}\left(X^2 + Y^2\right)\cos(2\omega t) + e\mathbf{f}(t)\cdot\mathbf{R}. \tag{3.12}$$

$H_{\text{CM}}$ describes the harmonic axial and transversal confinement of the center of mass (CM) motion with $\omega_z$ and $\omega_\rho$ the respective trap frequencies. The term $H_{\text{el}}$ represents the motion of the electron in the superimposed fields of the doubly charged ionic parent core and the trapping potential $\Phi(\mathbf{r},t)$. $H_{\text{CM-el}}$ takes into account the coupling between the external CM motion and the internal electronic dynamics. The last term $H_{\text{mm}}$ of the Hamiltonian describes the micromotion which causes a coupling between the static oscillator levels of $H_{CM}$. For the typically high values of the RF frequency $\omega$ it can be neglected.

Since we want to find out how the excitation into Rydberg states changes the trapping potential seen by the Rydberg ion, we only need to look at the coupling of the internal and external dynamics which is described by the term $H_{\text{CM-el}}$ (see equation 3.10). Since the electron dynamics takes place on a much faster timescale than the CM motion, the Born-Oppenheimer approximation is justified for treating this coupling. Diagonalizing this Hamiltonian and evaluating only the coupling of $|n,s\rangle$ and the next $|n,p\rangle$ levels with second-order perturbation theory over the average of one RF-cycle leads to an energy correction. This correction results in a modification of the transversal and longitudinal trap frequencies of ions in Rydberg states compared to ions in the ground state. These frequency shifts $\delta\omega_{\rho,z}$ scale with the principal quantum number as $\sim n^7$. For typical linear Paul traps, the field gradients $\alpha$ and $\beta$ are not equal. Normally, $\alpha \gg \beta$ is fulfilled, and thus the change of radial trapping frequency $\delta\omega_\rho$ is much larger[3]

[3] In [11] the shifts are calculated for a $^{40}\text{Ca}^+$ Rydberg ion with the principal quantum number $n = 50$ in a trap with $\omega = 2\pi \cdot 15\,\text{MHz}$, $\alpha = 10^9\,\text{V/m}^2$, and $\beta = 10^7\,\text{V/m}^2$ to be $(\delta\omega_\rho)/\omega_\rho = 3.5 \cdot 10^{-2}$ and $(\delta\omega_z)/\omega_z = 7.4 \cdot 10^{-4}$.

than for the axial frequency $\delta\omega_z$. Although this frequency shifts are negligible for low principal quantum numbers, due to the scaling of $\sim n^7$ they increase dramatically for higher excitation levels.

## 3.3 A two-qubit phase gate with Rydberg ions

There are several different proposals for qubit gates with trapped Rydberg ions, see for example [11] and [26]. In this section we want to look at one scheme for the implementation of a fast quantum gate with trapped Rydberg ions in more detail. This gate was first suggested by Jaksch et al. in 2000 for neutral Rydberg atoms [27], here it is applied to a system of trapped Rydberg ions.

The approach of Jaksch et al. relies on a phenomena called the Rydberg blockade. It is a result of the strong interactions between neighbouring Rydberg atoms (or ions). If one atom is excited to the Rydberg state by a laser pulse it will shift the Rydberg energy level of a neighbouring atom out of resonance with respect to the laser. Thus the second atom cannot be excited into the Rydberg state. The Rydberg interaction decreases with the distance, thus an atom at a larger distance will not be shifted out of resonance sufficiently to not be excited anymore. The transition point between these two regimes is called the *Rydberg blockade radius*. Figure 3.2 shows a graph explaining this behaviour.

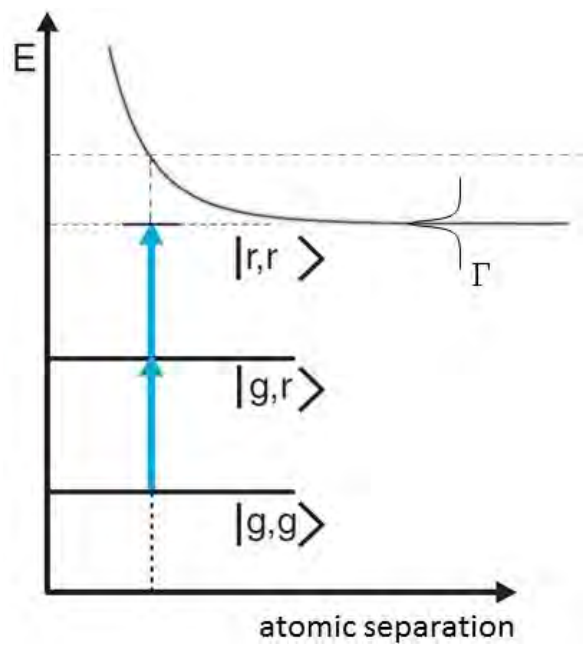


**Figure 3.2:** Energy level scheme for the Rydberg blockade between two atoms. The state |g,g⟩ denotes the case where both atoms are in the ground state. In |g,r⟩ one atom is excited into the Rydberg state, |r,r⟩ is the common state of two neighbouring Rydberg atoms. The energy level of this state |r,r⟩ depends on the distance between the atoms. For a separation smaller than the Rydberg blockade radius it is shifted out of resonance and thus |r,r⟩ cannot be excited.

We now want to show how a two-qubit phase gate can be realised with the Rydberg blockade. The key components are a two-atom system and a narrow laser which is only resonant to a single atomic transitions from an upper ground state $|0\rangle$ to a Rydberg state $|\mathrm{Ry}\rangle$, the lower ground state $|1\rangle$ is not resonant. For two atoms, there are four different initial combinations of upper and lower ground state occupation, each case is displayed in figure 3.3.

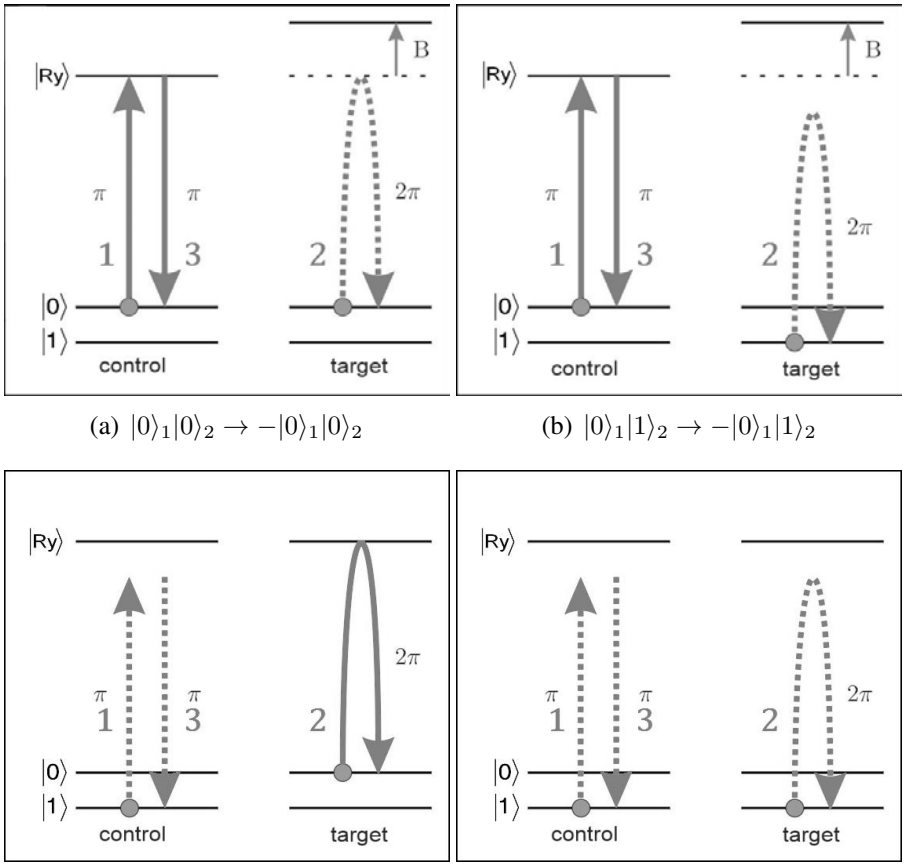


(a) $|0\rangle_1|0\rangle_2 \rightarrow -|0\rangle_1|0\rangle_2$ (b) $|0\rangle_1|1\rangle_2 \rightarrow -|0\rangle_1|1\rangle_2$

(c) $|1\rangle_1|0\rangle_2 \rightarrow -|1\rangle_1|0\rangle_2$ (d) $|1\rangle_1|1\rangle_2 \rightarrow |1\rangle_1|1\rangle_2$

**Figure 3.3:** Conditional two-qubit phase gate realised with the Rydberg blockade. The pulse-sequence is $\pi_{\text{control}} \rightarrow 2\pi_{\text{target}} \rightarrow \pi_{\text{control}}$. The details of the gate are explained in the text below.

The pulse sequence of the laser pulses is always the same: first a $\pi$-pulse is applied to the first qubit (the control qubit). Then a $2\pi$-pulse is applied to the second qubit (target qubit) and as the last step a second $\pi$-pulse is applied again to the control qubit. The reaction of the combined two-atom system to this sequence depends on the initial state population of the two atoms. If the system was initially in the state $|0\rangle|0\rangle$ (case (a)), the control qubit gets excited into the Rydberg state $|\mathrm{Ry}\rangle$ by the first $\pi$-pulse. Thus the target qubit is shifted out of resonance due to the Rydberg blockade and it is thus unaffected by the applied $2\pi$-pulse. The second $\pi$-pulse onto the control qubit returns it to the initial state. The whole system has gathered an additional sign change in the wave function. In case (b) the system is started initially in state $|0\rangle|1\rangle$. The target qubit is

again shifted out of resonance (it would be non-resonant even if it was not shifted) and as a result the wave functions gains a sign change equal to case (a). In the third case, shown in (c), the initial state of the system is $|1\rangle|0\rangle$. Here the control qubit is out of resonance for the Rydberg excitation, and thus cannot be excited into the Rydberg state $|\mathrm{Ry}\rangle$ by the first $\pi$-pulse. However, the target qubit is resonant to the $2\pi$-pulse which again causes a sign change to the system's wave function. The only case not gaining a phase change is shown in (d). Here the system is initially in state $|1\rangle|1\rangle$ and neither the control nor the target qubit are resonant to the $\pi$- and $2\pi$-pulses, respectively. Thus, no sign change accumulates.

The entire pulse-sequence corresponds to a controlled phase gate, where depending on the initial state of the control qubit the target qubit will be rotated by a $\sigma_z$ operation[4] or not. Since the shift of Rydberg energy levels can be on order of several megahertz and the lifetime of Rydberg states is in the microsecond regime, relatively high Rabi frequencies can be applied and thus the gate operation should take less than a microsecond.

[4] $\sigma_z = \begin{pmatrix} 1 & 0 \\ 0 & -1 \end{pmatrix}$

# Chapter 4

# Experimental setup

The aim of this experiment is to use trapped $^{88}Sr^{+}$ Rydberg ions for quantum computation. Strontium is a quite common alkaline earth metal. Like all alkaline metals it reacts easily with oxygen, nitrogen, sulphur and halogens. Strontium has four stable natural isotopes, $^{84}$Sr, $^{86}$Sr, $^{87}$Sr and $^{88}$Sr. $^{87}$Sr is the only fermionic isotope amongst them. The natural abundances of the isotopes in the order given above are $0.6\%$, $9.9\%$, $6.9\%$ and $82.6\%$.

This chapter explains the experimental setup that will be used for trapping $^{88}Sr^{+}$ ions and exciting them to Rydberg states. The outline of the chapter is as follows: in sections 4.1 the level scheme of $^{88}$Sr and $^{88}Sr^{+}$ is discussed. It then describes the transitions suitable for photoionisation of the atoms, as well as cooling, repumping and state manipulation of the trapped ions. The lasers used for the different tasks are shown. The second section covers the ion trap. The overall setup is explained and the various components including the electrode configuration and the trap-mount are covered in detail. The trapping parameters estimated for our system with $^{88}Sr^{+}$ are given. The third section deals with the vacuum chamber which houses the trap. The combination of all three systems of chamber, trap and laser apparatus is discussed. The main focus lies on the use of the different optical axes that are provided by the system. In section 4.4 the lens used for individual addressing of the ions is covered. The fifth and final section of this chapter describes the cleaning and bake-out procedure before dealing with the assembly of the ion trap and the vacuum chamber in detail.

## 4.1 Laser systems

In this first section the focus lies on the different transitions that are used for achieving ionisation, manipulation and excitation of confined $^{88}Sr^{+}$ ions. The laser wavelengths required for the different tasks are discussed, along with the experimental setup of the required laser systems. For an easier understanding the level-scheme is broken up into three parts, the ionisation of $^{88}$Sr atoms, manipulation (i.e. state preparation, laser cooling and repumping) and the Rydberg excitation. This approach is applied in the same way to the explanation of the laser systems.

### 4.1.1 The level-scheme

The level-scheme with the relevant transitions is shown in figure 4.1. To obtain ions, $^{88}$Sr atoms are emitted from a strontium source and ionised by photoionisation. The transitions used for ionisation are shown in red. The strontium source consists of two commercial ovens which are positioned directly below the ion trap and aim at its centre, see section 4.2. This two-photon ionisation process takes place by the absorption of one 461 nm photon which excites one of the two valence electrons into a P-state and a 405 nm photon which further excites the electron to an autoionising state above the ionisation limit. The 461 nm laser is a commercial system while the 405 nm light is emitted by a standard Blu-ray laser diode. The setup for these lasers can be seen in figure 4.3. Since no narrow bandwidths are required, neither of the lasers are stabilised to a cavity.

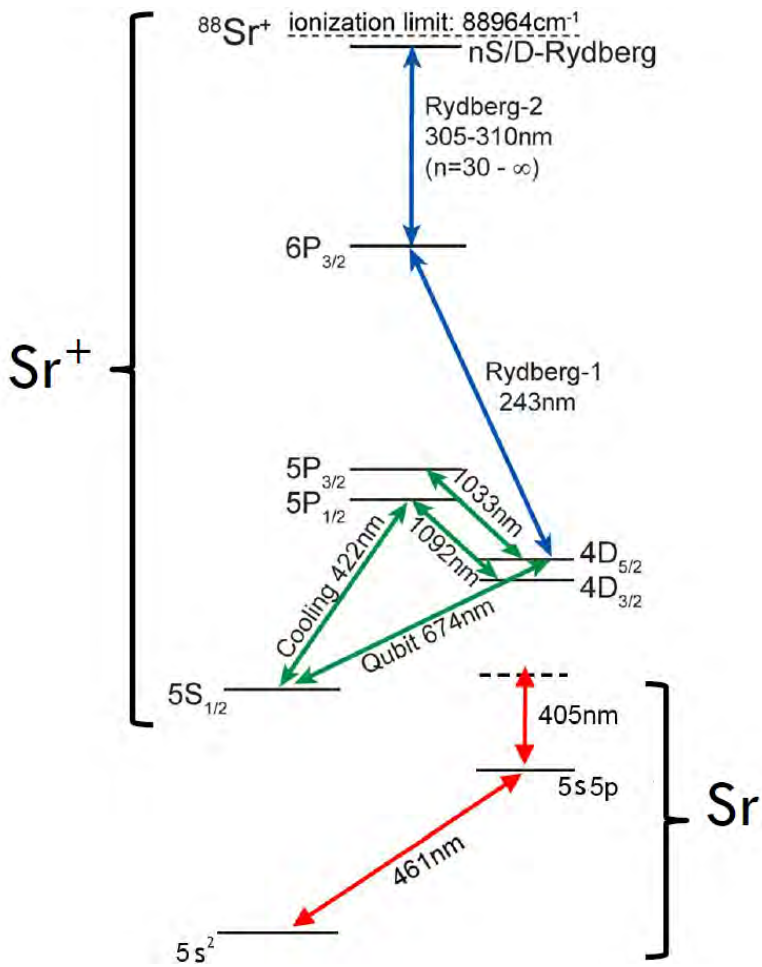


**Figure 4.1:** Level-scheme for $^{88}$Sr. The red arrows denote the laser transitions for photoionisation of the neutral Sr atom, green for cooling, repumping and qubit state manipulation of the $^{88}$Sr$^{+}$ ions, and blue for Rydberg excitation. Except for the Rydberg transition, all lasers are diode lasers. The wavelengths required for the Rydberg excitation are achieved by frequency doubling and sum-frequency generation of diode lasers partially amplified by fibre lasers. The ionisation limit of 88964 cm$^{-1}$ with respect to the $5S_{1/2}$ ground state is shown in the scheme.

Cooling, state preparation, qubit manipulation, and repumping of trapped ions is done with transitions shown in green in figure 4.1. All four wavelengths (422 nm, 674 nm, 1033 nm, and 1092 nm) are commercial diode lasers. The 422 nm laser is used for both Doppler cooling ions and fluorescence detection of the $5S_{1/2}$ state. The 674 nm light is employed for qubit manipulation and in combination with the 1033 nm for sideband cooling. The 1033 nm laser light is needed in the sideband cooling scheme because the $4D_{5/2}$ state has a quite long lifetime that would make sideband cooling very slow. Thus we have a three-level sideband cooling where the 1033 nm laser quenches the $4D_{5/2}$ state via the $5P_{3/2}$ state. During cooling and state detection with the 422 nm laser the probability of the state $5P_{1/2}$ to decay into the long-lived state $4D_{3/2}$ is not negligible, thus we require 1092 nm laser light for repumping the ions from this state back to the 422 nm cycling transition.

To excite an ion into the Rydberg state requires photons with high energy. In the case of our $^{88}Sr^+$ ions the energy needed to excite the ion from the metastable $4D_{5/2}$ state to the Rydberg state corresponds to a single photon of 135 nm wavelength. Laser light of this wavelength is very difficult to handle since it is absorbed in air, thus requiring the whole setup to be in vacuum. While the approach of Rydberg excitation with one photon is possible[1], in our case a two-photon excitation is more feasible because the required wavelengths are above the vacuum-UV regime. In the first step of the two-photon excitation, the valence electron of the trapped $^{88}Sr^+$ ion will be excited from the $4D_{5/2}$ state to the $6P_{3/2}$ state with a photon of 243 nm wavelength. From this state a second photon will excite it into the Rydberg state. The wavelength of this photon can be adjusted between 305 nm to 310 nm. This variation in energy allows excitation of different Rydberg states, from states of principle quantum number $n = 30$ up to double-ionisation of the $^{88}Sr$ atom.

### 4.1.2 Setup of the laser systems

The following section summarises and shows the laser systems for ion and atom manipulation. The description of the systems is split in three parts (ionisation, ion manipulation and Rydberg excitation) as in the section above.

#### Ionisation lasers

As previously stated, the ionisation of $^{88}Sr$ atoms is performed in a two-photon ionisation process. There are several reasons why we prefer photoionisation over the more traditional method of electron bombardment [28, 29]. One significant drawback when using electron bombardment in experiments with ion traps is the charging of nearby surfaces due to the use of an electron gun. Since these charges vary with time, one needs to apply frequent micromotion compensation for the additional electric fields.

[1] An experiment realising a one-photon Rydberg excitation of trapped $^{40}Ca^+$ ions is currently being set up at the Institute für Physik from the Johannes Gutenberg-Universtität in Mainz by the groups of Ferdinand Schmidt-Kaler and Jochen Waltz [25]. Although double-ionisation was shown, no Rydberg excitation has been reported at the time writing.

Another disadvantage is that the atomic beam density required for ionisation with electron bombardment is roughly a factor of $10^4$ larger than compared to the densities that are required for photoionisation. Thus photoionisation helps to significantly decrease the amount of strontium that is deposited onto the blade electrodes, further reducing stray fields inside the trap. One final advantage of photoionisation worth mentioning is that it allows element selective and even isotope selective ionisation, making the production of high-purity ion crystals much easier.

Strontium offers several different ionisation schemes of which three are displayed in figure 4.2. Since both wavelengths of the ionisation process in figure 4.2 (a) are commercially available it's the transition scheme we have chosen to use. The first excitation is driven by a system[2] which gives around $15\,\mathrm{mW}$ of light at $461\,\mathrm{nm}$. The $405\,\mathrm{nm}$ light is provided by a standard Blu-ray laser diode and gives approximately $100\,\mathrm{mW}$ of light for exciting the $^{88}$Sr atom into the autoionising $\left(4d^2+5p^2\right)\ {}^1D_2$ state. Since both lasers are needed for the ionisation and are never used separately, both beams are coupled into the same fibre.

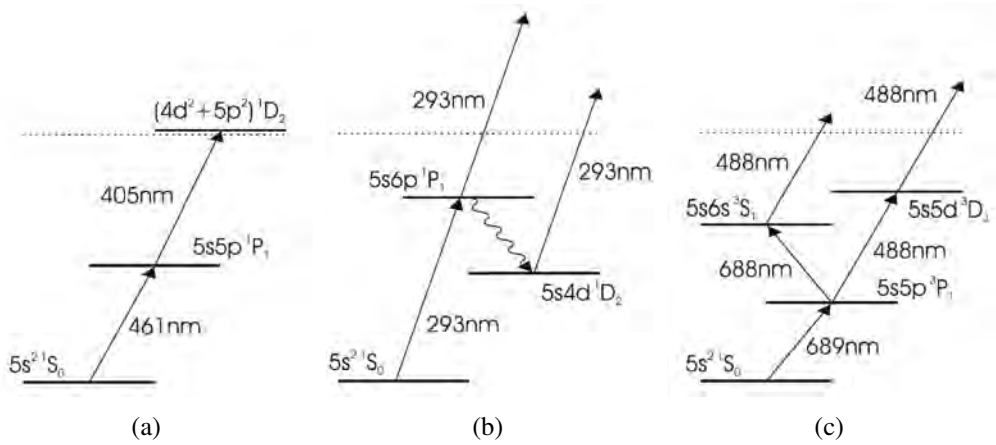


(a) (b) (c)

**Figure 4.2:** Possible schemes for two-photon ionisations processes in strontium [29]. In our experiment we use scheme (a). The atom is first excited with a $461\,\mathrm{nm}$ photon via the $5s^2\,{}^1S_0 - 5s5p\,{}^1P_1$ dipole transition. A second photon with the wavelength of $405\,\mathrm{nm}$ excites the atom further into the autoionising $\left(4d^2+5p^2\right)\ {}^1D_2$ state.

Figure 4.3 shows the experimental setup of the ionisation lasers. Both beams are handled the same way: after leaving the laser, the beams are shaped with a pair of cylindrical lenses. To couple them into a collimator, telescopes consisting of two spherical lenses are used for mode-matching. On a polarising beam splitter (PBS) cube the beams are overlapped before coupling into the fibre. Since a narrow laser linewidth is not important for two-photon ionisation, the lasers don't need to be additionally stabilised to a cavity. A wavemeter is accurate enough for matching the $461\,\mathrm{nm}$ laser to the $^{88}$Sr resonance.

[2]Toptica DL 100 pro

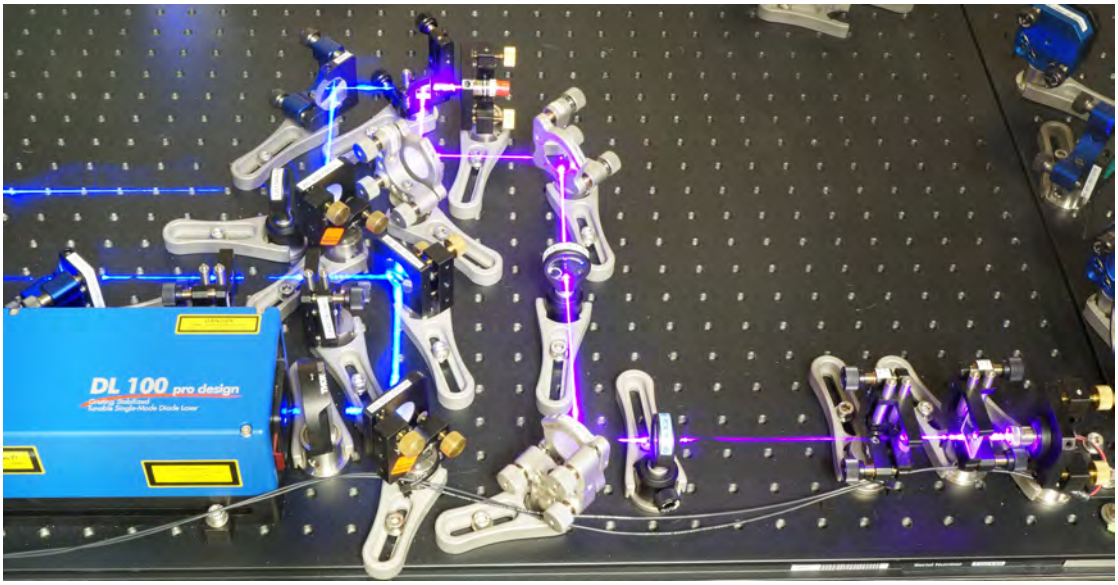


**Figure 4.3:** Experimental setup of the photoionisation lasers. The 461 nm laser (Toptica DL100 pro design, blue beam) on the left hand side and the 405 nm Blu-ray laser diode (purple beam) on the right hand side are overlapped with orthogonal polarisations on a polarising beam splitter cube (upper center). In the picture, the fibre that guides the light to the vacuum chamber and the trap is not attached to the collimator. The laser beams seen in the picture were made visible by following the beam path with an lens-cleaning tissue while taking a long-exposure photograph.

### Lasers for Doppler cooling, repumping and state manipulation

All four wavelengths required for standard quantum information processing of the trapped ions are commercial diode laser systems. At the time of writing, the 674 nm laser[3] used for state manipulation and sideband cooling is yet to be set up, so this section focuses on the three lasers used for Doppler cooling and repumping.

After ionisation the trapped ions are hot. Figure 4.4 shows the level-scheme used to Doppler cool the Sr ions [29, 30]. A laser with a wavelength of 422 nm drives the ${}^2S_{1/2} \rightarrow {}^2P_{1/2}$ transition, which has a natural linewidth of $\Gamma/2\pi = 20.2$ MHz. Besides Doppler cooling, this transition is used for state detection. Since the ${}^2P_{1/2}$ state can be lost from the cooling cycle by a decay into the metastable ${}^2D_{3/2}$ state we use a 1092 nm laser for repumping.

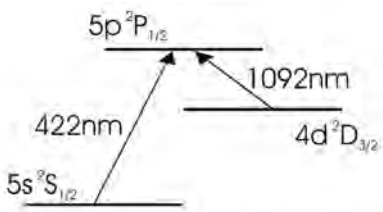


**Figure 4.4:** Transitions that can be used for Doppler cooling [29].

[3]Toptica DL 100 pro, 500 mW output power

The 422 nm laser is also a commercial diode laser[4]. The wavelength for Doppler-cooling of $^{88}$Sr ions via the $5S_{1/2} \rightarrow 5P_{1/2}$ transition is 421.67067 nm[5]. In order to lock the laser to this wavelength we exploit the fact that the $5s\,^2S_{1/2}\,(F=2) \rightarrow 6p\,^2P_{1/2}\,(F'=3)$ transition of the $^{85}$Rb isotope lies only about 440 MHz away from the resonance frequency of the $^{88}$Sr$^+$ cooling transition. This allows us to stabilise the laser with a suitable spectroscopy setup. We use a glass cell filled with Rb gas to perform Doppler-free absorption spectroscopy and obtain an error signal that allows locking onto the Rb transition. Before shining the stabilised laser light onto the ions, its frequency is shifted with acousto-optic modulators (AOM) to match the wavelength of the $^{88}$Sr$^+$ Doppler cooling transition. Figure 4.5 shows the experimental setup of this step. Setting up this part of the experiment was also part of a students' project, see [31] for a more detailed discussion.

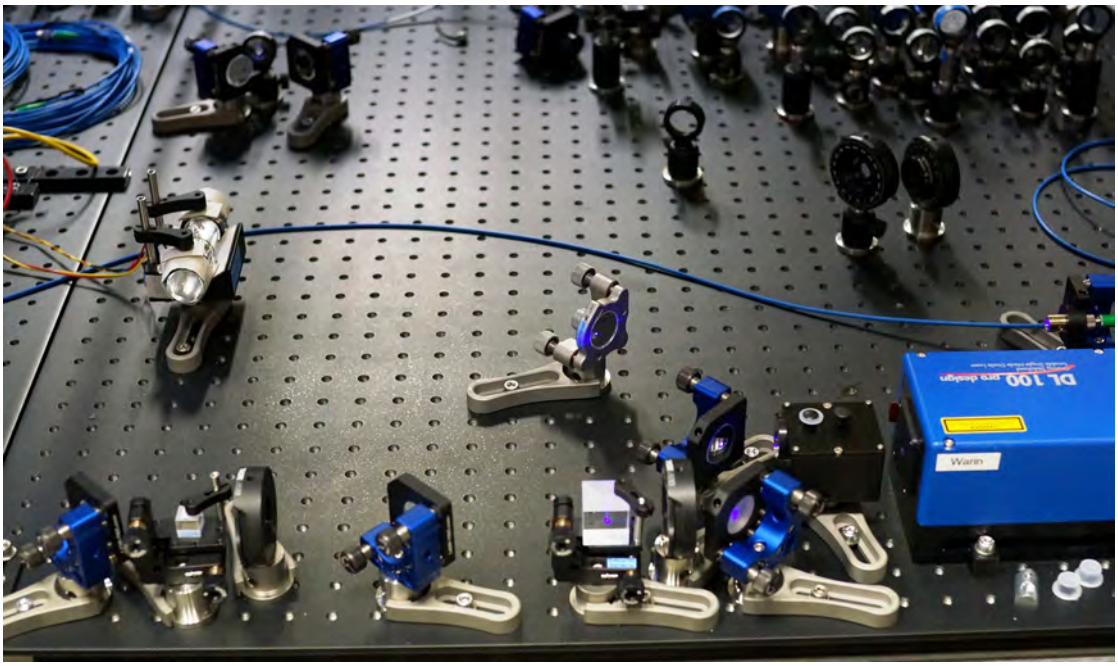


**Figure 4.5:** Experimental setup of the 422 nm laser and the rubidium cell for saturated absorption spectroscopy. In the lower right corner the laser can be seen, followed by an anamorphic prism pair for beam-shaping. Some light is separated with a polarising beam splitter cube and sent through a rubidium cell, which can be seen on the left of the picture. The rubidium cell is heated to increase the vapour pressure and thus the size of the error signal for laser stabilisation.

For repumping from the metastable $^2D_{3/2}$ state, which is populated during Doppler cooling, laser light at a wavelength of 1092 nm is required[6]. A schematic drawing of the setup can be seen in figure 4.6. The laser beam is shaped with an anamorphic prism pair mounted in the casing of the laser (in contrast to the 422 nm setup seen in figure 4.5 where these prisms are mounted in a black box in front of the laser). After the standard setup of two mirrors, which allow alignment of the beam direction, a polarising beam

[4]Toptica DL 100 pro, 50 mW output power
[5]http://physics.nist.gov/PhysRefData/Handbook/Tables/strontiumtable4.htm
[6]Toptica DL 100 pro, 120 mW output power

splitter cube in combination with a $\lambda/2$ plate is used to branch off some light (around $1.7\,\mathrm{mW}$). The splitting ratio can be adjusted via the waveplate. This light is again split with a beam sampler and each resulting beam is coupled into a fibre. One fibre leads to a wavemeter while the other goes to a stabilisation cavity in a Pound-Drever-Hall (PDH) configuration [32]. The photodiode signal from the PDH setup is fed directly to the digital control unit of the laser[7]. This control unit allows stabilisation of the laser via a computer program without the need of further electronics[8].

The main part of the light leaves the PBS in reflection and is reflected by a further PBS cube and sent to an acousto-optic modulator. This AOM is used to control the laser frequency and power sent to the ion trap and is set up in double-pass configuration. A $\lambda/4$ plate after the AOM causes a $90°$ rotation of the polarisation after the double pass so that the beam now goes through the PBS cube in transmission. The light is then coupled into a fibre and sent to the vacuum chamber. Figure 4.7 shows a photograph of the setup. Please note that the PDH setup and the cavity are not shown in this picture.

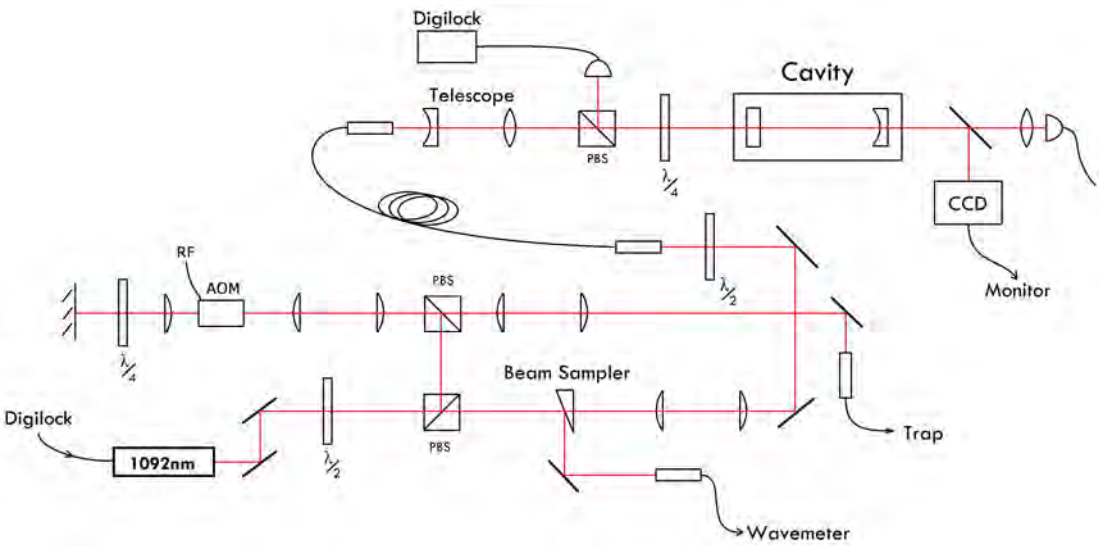


**Figure 4.6:** Schematic of the $1092\,\mathrm{nm}$ laser setup. Some light is split off with a PBS and sent to a wavemeter and to a medium-finesse cavity in a PDH setup for stabilisation. The resulting error signal is generated and processed in the laser's own control unit and requires no further electronics. The light transmitted by the cavity is split with a beam sampler. One part is sent onto a CCD (from a normal webcam with optics removed) and allows observation of the cavity mode. The second part measures the cavity transmission on a photodiode. The majority of the light coming from the laser and passing the first PBS in reflection is sent to a second PBS and through an AOM in a double-pass configuration. The frequency-shifted light is coupled into a fibre and sent to the vacuum chamber with the ion trap.

[7] Toptica Digilock

[8] Usually PDH electronics consists of the PDH modulation, the demodulation and the PID controller for feedback. The digital controller includes these three functions in one device.

**Figure 4.7:** Photograph of the 1092 nm laser setup. The configuration follows the schematics in figure 4.6 although for practical reasons the spatial assembly varies to some degree. In the upper left corner one can see the AOM and the optics needed for the double-pass configuration. In the lower right corner two collimators are located leading to the wavemeter (orange fibre) and the ion trap, respectively. The collimator in the upper middle of the picture leads to the cavity. Note that the cavity itself and the PDH setup are not shown in the photograph.

The 1033 nm laser[9] used for sideband cooling is set up in the same way as the 1092 nm laser. Figure 4.8 shows the experimental configuration, the schematic setup is the same as in figure 4.6.

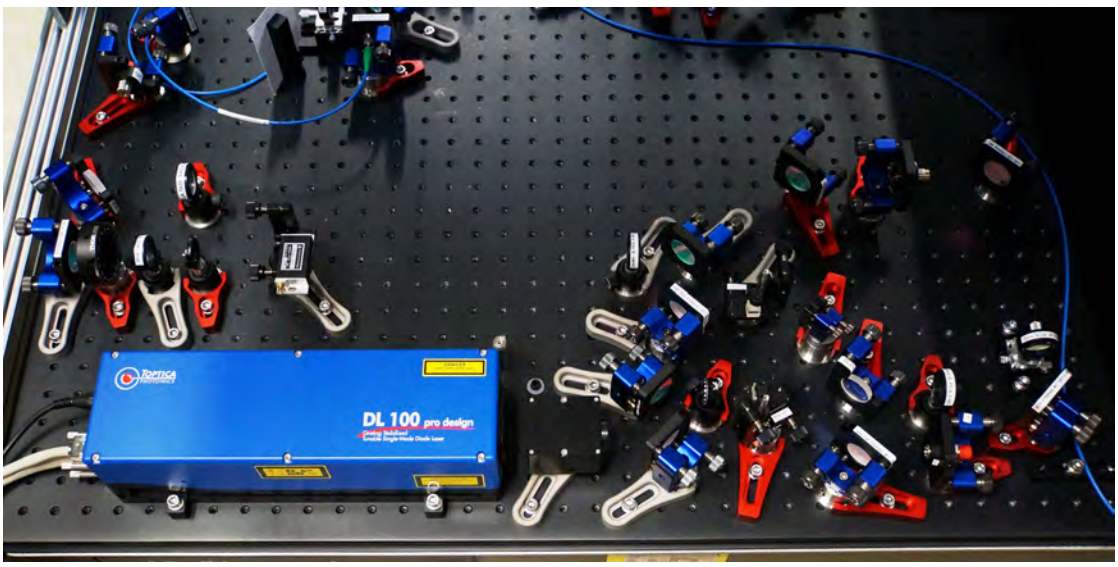


**Figure 4.8:** Photograph of the 1033 nm laser setup. The configuration follows the schematic in figure 4.6.

[9]Toptica DL 100 pro, output power 80 mW

### Laser system for Rydberg excitation

As already stated at the beginning of this chapter, the excitation of a $^{88}Sr^{+}$ ion to a Rydberg state requires a relatively large amount of energy. Even with a two-photon process the required wavelengths of $243$ nm and $305$ nm $-$ $310$ nm are in the UV regime. Neither of the wavelengths can be produced by a diode laser but rather are generated through second harmonic generation (SHG) and sum-frequency generation (SFG). The experimental setup for generating the required lasers are key components of our experiment and the subject of a master project carried out by Christine Maier. On the following pages I will summarise the setup and refer the interested reader to this master thesis for a more detailed discussion of the topic [33].

SFG and SHG are nonlinear optical effects that occur in nonlinear optical media at hight light intensities. While a weak light field induces a polarisation $P(t) = \chi^{(1)} E(t)$ which depends linearly on the electric field $E(t)$, a strong light field induces a polarisation of the form

$$P(t) = \chi^{(1)} E(t) + \chi^{(2)} E^2(t) + \chi^{(3)} E^3(t) + \dots \quad , \tag{4.1}$$

where $\chi^{(2)}$ and $\chi^{(3)}$ are the second- and third-order nonlinear optical susceptibilities. Second-order nonlinear optical effects can only occur in optical materials which lack central symmetries, for example, beta-barium borate (BBO), lithium triborate (LBO), and lithium niobate (LN). Materials which show inversion symmetry like gases, liquids, amorphous solids, and many crystals don't show second-order nonlinear optical effects.

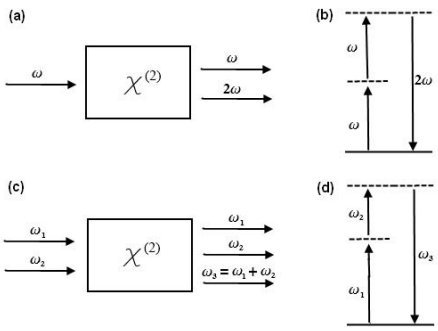


**Figure 4.9:** Schematics for second harmonic generation (a) and sum-frequency generation (c) ((b) and (d) show the energy-level diagram for the respective nonlinear optical effect). The processes can be understood as follows: for SHG two photons of the same frequency are annihilated by the optical material and a new photon with double the frequency is emitted. In SFG two photons of different frequencies are annihilated and a new photon with a frequency given by the sum of the frequencies is generated. Thus one can see that SHG is a special case of SFG in which $\omega_1 = \omega_2$.

The basic principles of second harmonic generation and sum-frequency generation are shown in figure 4.9. For SHG one can treat the process as an annihilation of two photons with frequency $\omega$ and the creation of a new photon with frequency $2\omega$, as shown in figure 4.9 (a) and (b). In the case of SFG the incoming light field consists of the

two different frequency components $\omega_1$ and $\omega_2$. For such an incoming light field with two frequency components, four different second-order nonlinear effects may occur. Namely sum frequency generation, difference frequency generation, second harmonic generation or optical rectification. The fields produced by each of these effects have frequencies $\omega_1+\omega_2$, $\omega_1-\omega_2$ and $\omega_2-\omega_1$, $2\omega_1$ and $2\omega_2$, and zero frequency, respectively. In general, the different processes are not optimised simultaneously and thus the radiation intensities for the different frequencies can only be maximized one at a time. The process favoured depends on the phase-matching condition, which is related to momentum conservation and is, in general, different for each of the processes.

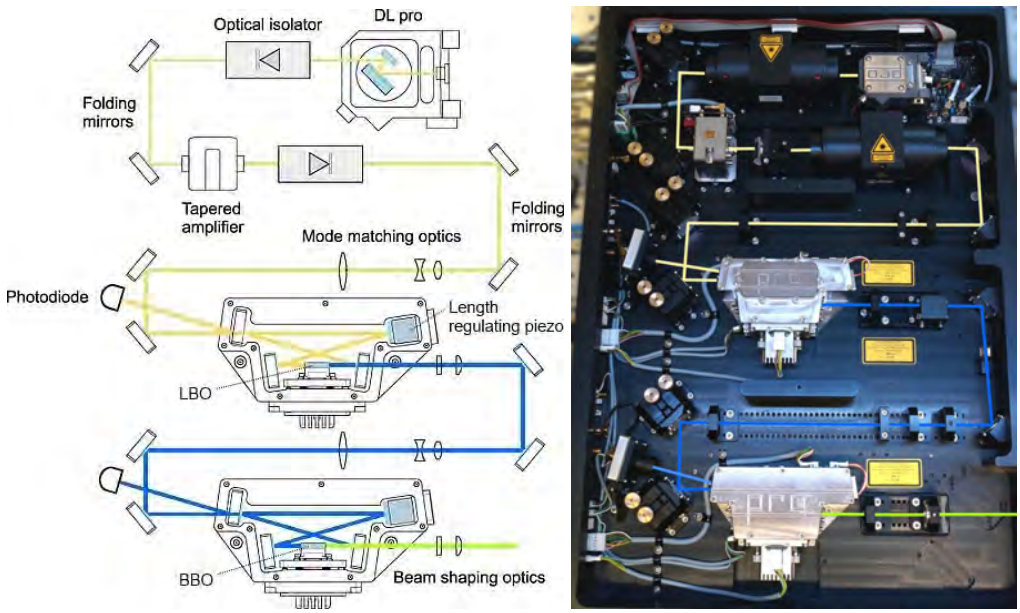


(a) (b)

**Figure 4.10:** (a) Schematics of the 243 nm laser. (b) shows the actual setup. For clarification, each of the light-paths in the photograph is added in the same colour as used in the schematic. The setup includes two optical isolators which protect the laser diode and the tapered amplifier from back-reflections [33].

As already stated, we use both SFG and SHG to generate the wavelengths required for Rydberg excitation. The system for generating 243 nm light for the $4D_{5/2} \rightarrow 6P_{3/2}$ transition is a commercial system[10], see figure 4.10. In this system, a diode laser (stabilised with a grating) provides around 38 mW of 972 nm light which is amplified to around 620 mW with a tapered amplifier. A LBO crystal in a ring resonator is used to produce around 210 mW of 486 nm light via SHG. This light is again frequency doubled using a BBO crystal in a second ring resonator, thus finally generating the required light at 243 nm. Depending on the current applied to the tapered amplifier the 243 nm light output power should be able to reach up to 100 mW.

[10]Toptica TA/DL-FHG pro

While the generation of 243 nm light is not an easy or uncomplicated task, since the whole setup is commercially available, its implementation in the experiment is quite straightforward. The laser light required for the second excitation step from $6P^{3/2}$ to a Rydberg state is far more demanding: for coherent excitation of the Rydberg state the linewidth needs to be smaller than $\lesssim 100$ kHz. Furthermore, we want to be able to tune the light between 305 nm and 310 nm so that Rydberg states with $30 < n < \infty$ may be excited. The idea behind this laser system is to mix a laser, highly tunable between 998 nm and 1029 nm, with laser light at 1550 nm via SFG. The resulting laser light is variable between 607 nm and 619 nm. Frequency doubling of this light through SHG leads to the final wavelength which is tunable between 304 nm and 310 nm.

The tunable 1000 nm laser[11] offers a maximum output power of 1.5 W after the built-in tapered amplifier. The second fundamental beam is supplied by a 1551 nm diode laser[12]. It is 8 kHz broad and amplified by a fibre amplifier[13] to a maximum output power of 10 W. Figure 4.11 shows a schematic of the experimental setup. In the following few paragraphs the setup that gives us the light at the required UV wavelength is explained.

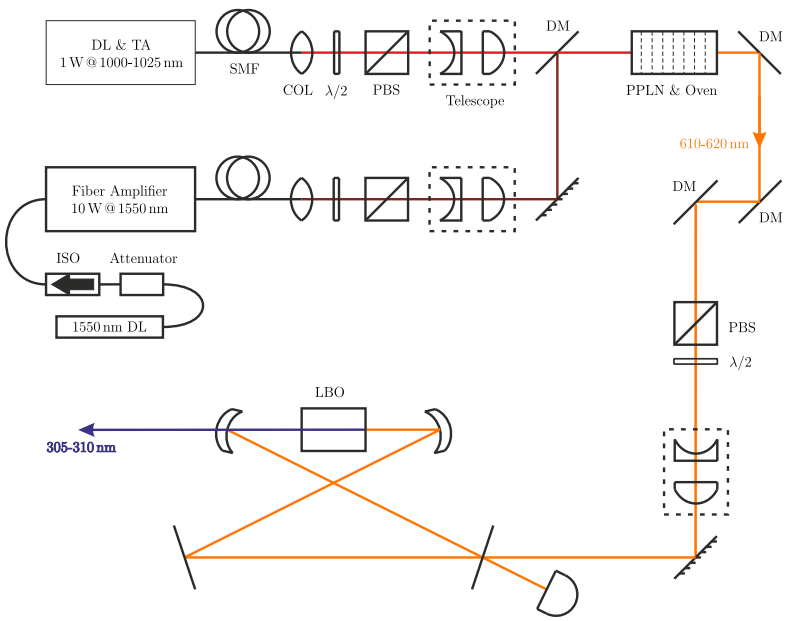


**Figure 4.11:** Schematics of the setup for generating 305 nm − 310 nm laser light via SHG and SFG. A 1551 nm and a tunable 1000 nm fundamental beam are overlapped and sent in single path through a PPLN crystal inside an oven. The resulting 607 nm − 619 nm beam is filtered with dichroic mirrors and coupled into a fibre (not shown). The following ring cavity with LBO crystal converts the light by second harmonic generation to the final UV wavelength at 304 nm − 309 nm [33].

[11] Toptica TA pro
[12] TeraXion PS-NLL
[13] Manlight CW fiber amplifier, type ML10-EYFA-CW-SLM-P-TKS

The output of the 1551 nm amplifier is directly fibre coupled and thus the beam has a well-defined Gaussian shape. The 1000 nm light, however, leaves its housing in free space. To get rid of distortions caused by the tapered amplifier, the light is first coupled into a single-mode fibre for mode filtering. Both lasers are sent through polarising beam splitter cubes so that the polarisation axes are vertical with respect to the optical table. To achieve the optimal conversion efficiency in the PPLN crystal the beams are sent through telescopes to meet the Boyd-Kleinmann conditions in the crystal. They are then overlapped on a dichroic mirror and sent into the crystal such that their beam waists are in the center of the crystal's length. Since the conversion efficiency is temperature-dependent, the crystal is housed inside an oven. After the crystal, the converted 607 nm to 619 nm light is separated from the fundamental beams via three dichroic mirrors. Before coupling into a fibre, the light produced is sent through a PBS. The photograph seen in figure 4.12 shows the experimental setup explained so far.

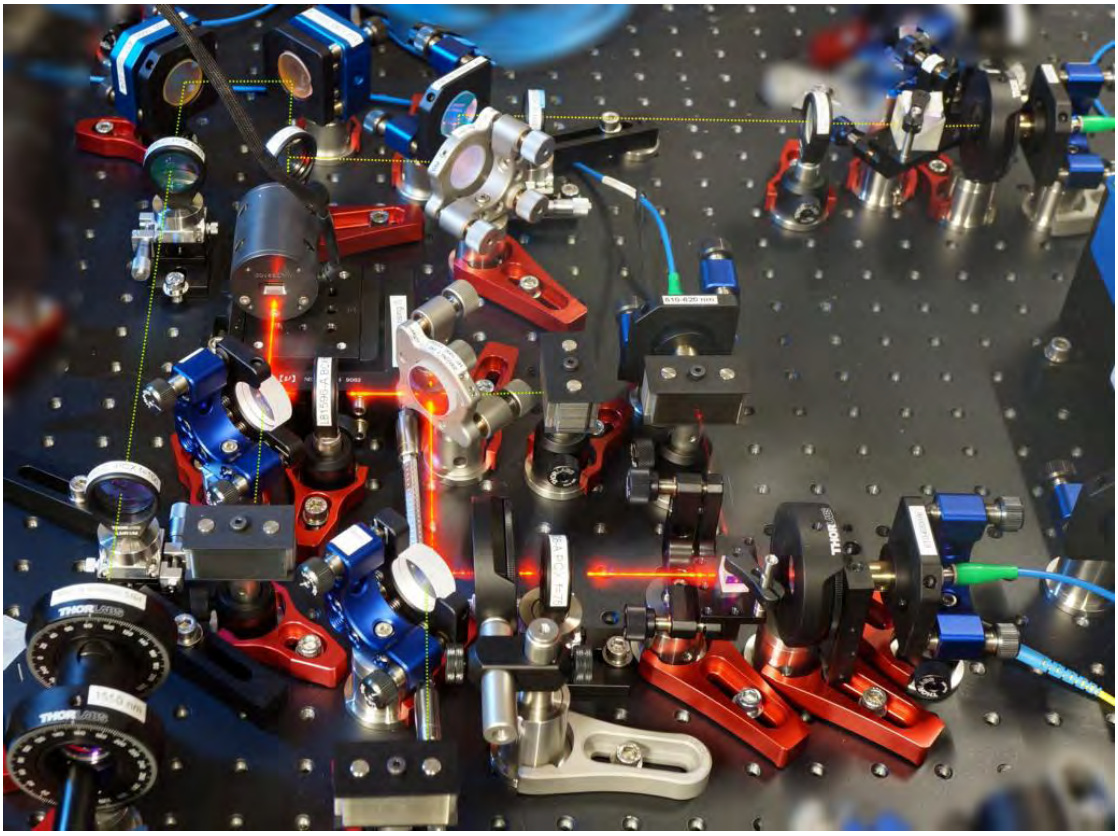

**Figure 4.12:** The SFG setup for production of the 607 nm − 619 nm light. In the lower left corner the 1551 nm beam leaves the collimator, indicated by the dashed green line. The tunable 1000 nm beam leaves the fibre used for mode filtering in the upper right corner indicated by a dashed yellow line. The beams are overlapped and sent into the PPLN crystal housed in the black cylindrical oven in the upper left corner of the photograph. The resulting 610 nm light beam is made visible with the same method used in figure 4.3. This light is separated from the fundamental beams using dichroic mirrors and coupled into a fibre in the lower right corner.

In the last step the 607 nm − 619 nm light is converted to UV light in a commercial SHG device[14] consisting of a LBO crystal mounted inside a ring cavity. A schematic and a photograph of the system can be seen in figure 4.13 (a) and (b), respectively.

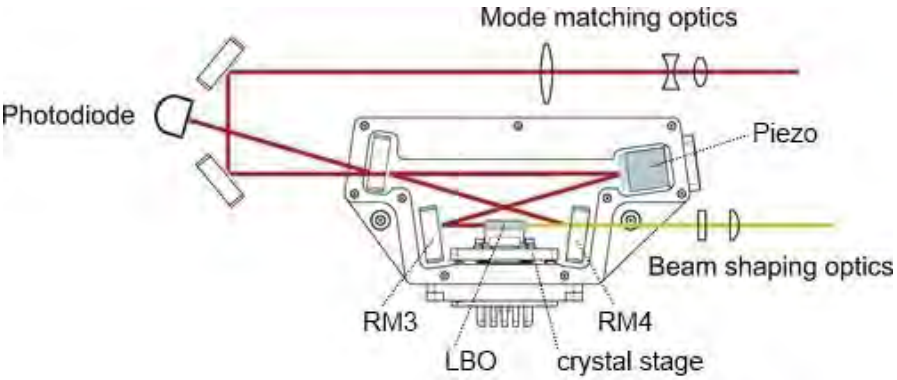


(a)

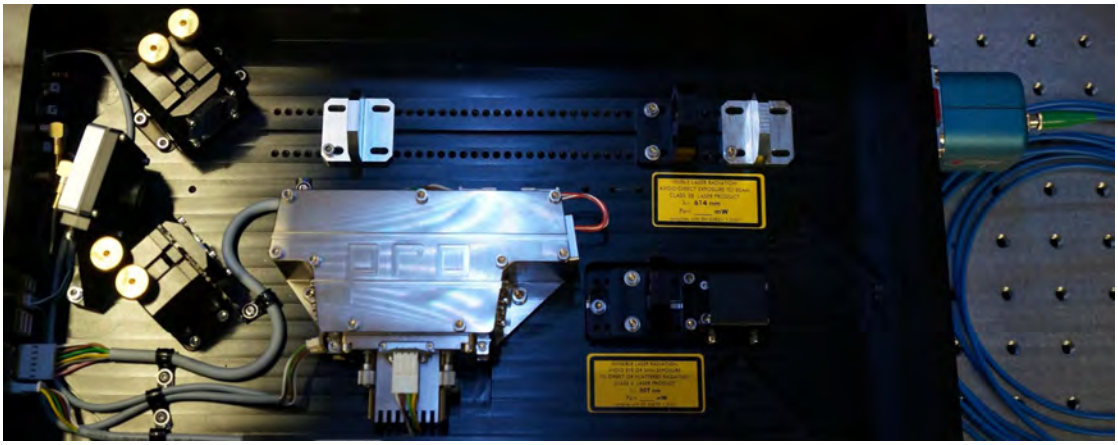

(b)

**Figure 4.13:** Schematic and a photograph of the doubling cavity used for converting the 607 nm − 619 nm light (red line) to the 304 nm − 310 nm UV light (green line). The incoming light is mode-matched with the ring cavity via lenses. The UV light is also beam-shaped before leaving the housing to compensate for astigmatism [33].

In a first test with an input power of 260 mW of 612 nm a light conversion efficiency of around 30 % could be achieved. These values translate to an output of 75 mW at 306 nm which is more than sufficient for the power for the Rydberg excitation (calculated to be roughly 5 mW). Tuning the wavelength of the 1000 nm fundamental beam and thus of the UV light requires temperature tuning and angle tuning of the SHG crystal to maintain the phase-matching conditions for optimal conversion efficiency.

[14]Toptica SHG pro

## 4.2 The ion trap

For trapping $^{88}Sr^+$ ions we will use a linear Paul trap. This trap is a standard macroscopic blade trap similar to others used in other experiments here in Innsbruck, however with a newly implemented design as discussed below. Another trap of the same kind is already set up and trapping $^{40}Ca^+$ ions in an atomic clock experiment at the Institute for Quantum Optics and Quantum Information (IQOQI), located in Innsbruck. The working principles of a linear Paul trap were explained in section 2.2, for a reminder of the general design see figure 2.2. In the following section our ion trap is shown and discussed. Since we know the parameters for trapping $^{40}Ca^+$ ions from the other experiment we can calculate the expected parameters for trapping $^{88}Sr^+$ ions. In the final part of this section, the strontium ovens placed in the hollow base of the trap mount are discussed.

The main difference between the new trap design and older blade traps are the used materials. In previous traps stainless steel and Macor[15] were used for the electrodes and the insulating holder, respectively. The new design uses titanium and sapphire instead. The four blade electrodes and the two endcap electrodes forming the trap are shown in figure 4.14 (a) and (b). They are made out of titanium as is the trap mount which houses the trap as well as the strontium ovens. The compensation electrodes are made out of stainless steel. All titanium parts were machined in the fine-mechanics workshop at the IQOQI. The insulating holder for the electrodes consists of three pieces of sapphire, see figure 4.14 (e). The photograph in figure 4.15 shows the assembled setup (the assembling process is explained in section 4.5). There are three main reasons why a combination of titanium and sapphire was chosen for the new trap design. Firstly, titanium and sapphire offer a higher thermal conductivity than stainless steel and especially Macor. The radiofrequency current in the trap electrodes usually heats up the trap significantly (to more than $100\,°C$ in old traps). The higher thermal conductivity enhances the coupling to the environment and thus lowers the trap temperature. Secondly, both titanium and sapphire absorb less of any present RF field. Thus, the RF field forming the trapping potential does not heat the setup as much compared to traps built from the "more traditional" materials. Thirdly, the thermal expansion coefficients of titanium and sapphire are more similar than those of Macor and stainless steel. Thus temperature changes will cause less stress in the setup. All these factors give rise to a superior thermal behaviour of the new design.

Before assembling the trap, all parts were thoroughly cleaned to make sure everything was free from grease and other kinds of dirt, see section 4.5.1 for a detailed description of the process. After cleaning, the blade and the endcap electrodes were electroplated with a gold layer around $20\,\mu m$ thick (one of the compensation electrodes was also gold-plated but the gold had to be removed during assembly to fit through the sapphire holder). The reason for the gold plating is to reduce electrical losses since the electrical conductivity of gold is around 20 times higher than that of titanium [34]. A

[15] Macor is a machinable glass-ceramic and a good thermal and electrical isolator. Due to its low outgassing rate it is often used in UHV applications.

second reason for the gold plating is the higher work function[16] of gold compared with titanium. Since the 243 nm laser with a photon energy of 5.10 eV has the lowest wavelength (and thus the most energetic photons) in our setup, all materials near the trapping center that could be hit by these photons should have a work function higher than this value.

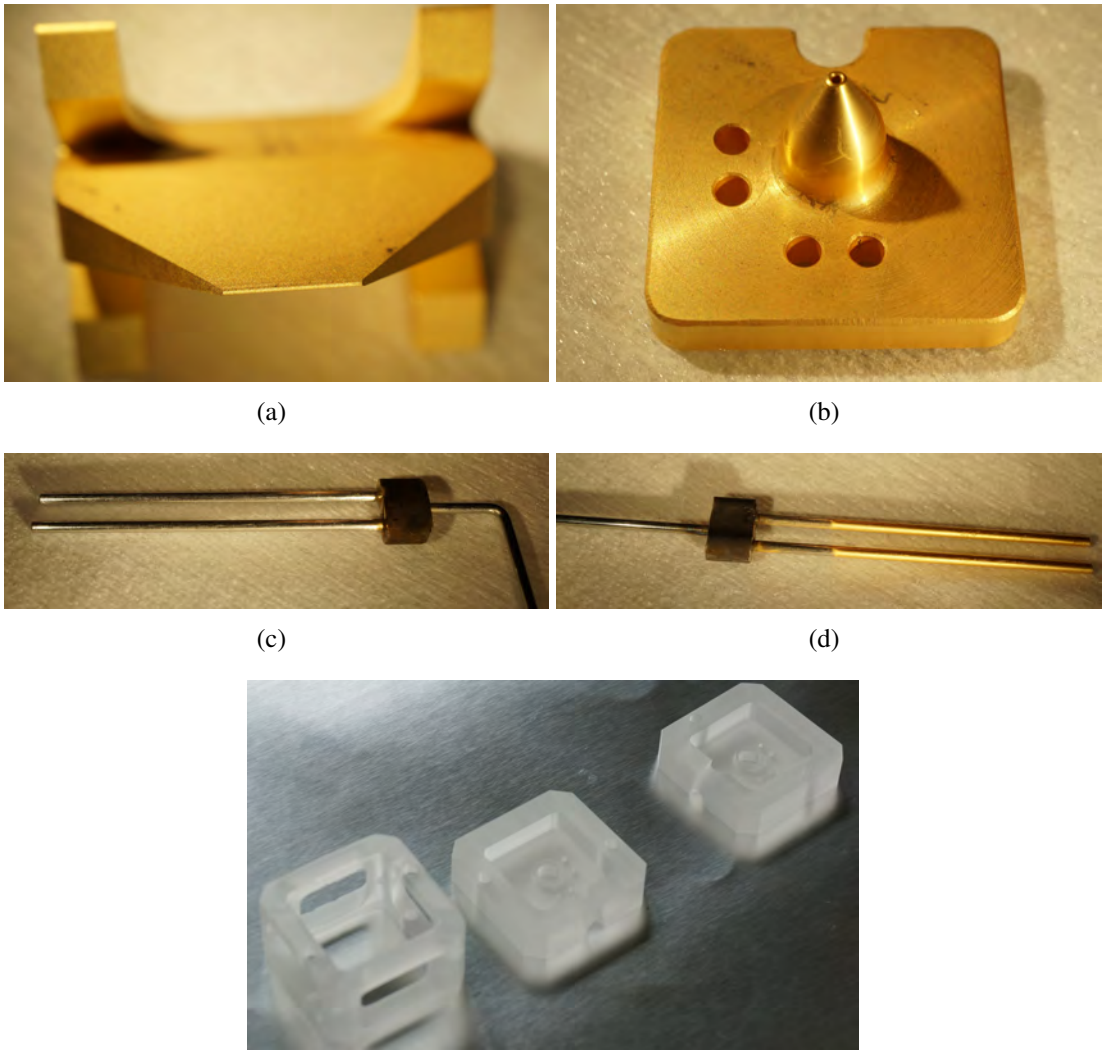


**Figure 4.14:** Picture (a) and (b) show a blade electrode and an endcap electrode, respectively. Both electrodes are made out of titanium and plated with gold. The tip of the endcap electrode has a hole completely drilled through so that a laser beam can be sent through the endcaps into the trap. This additional optical axis allows global addressing of ions trapped in a linear chain. The four holes on the side of the endcap electrodes are left for the compensation electrodes, shown in (c) and (d), to pass through. In (e) one can see the three sapphire pieces forming the insulating holder for the electrodes. The piece on the left hand side of the picture houses the blade electrodes while the other two pieces hold the endcap electrodes in place.

[16]The electron work function describes the minimum energy required to remove an electron from the surface of a solid material. Its value depends on the material, structure and purity [35].

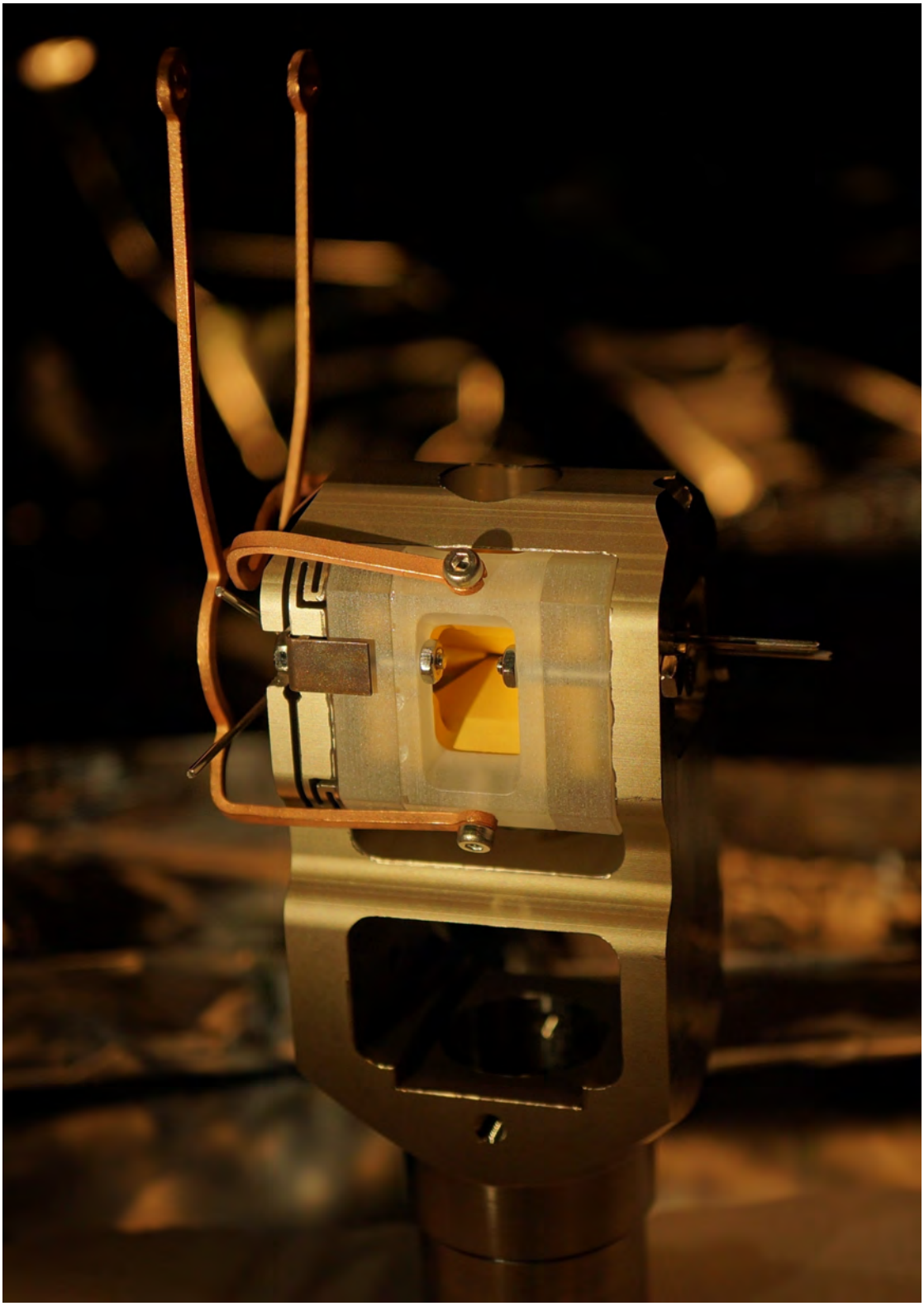

**Figure 4.15:** Complete ion trap assembly ready for mounting in the vacuum chamber. On the upper right corner of the trap mount the bore for the trap's third optical axis can be seen. Additional optical access to the trap is provided by a hole in the center of top of the trap mount. The lower part of the trap mount is hollow. This is where the strontium ovens are mounted.

Titanium has a work function of $\Theta = 4.33\,\text{eV}$ [34] and thus electrons can be extracted if $243\,\text{nm}$ photons hit the surface of the bare electrodes. This could lead to both unwanted free electrons in the trapping region and the development of uncontrollable charged regions on the surface of the blade electrodes. Both effects disturb the trapping potential as well as the ions and could be an additional source of ion heating. Pure gold on the contrary has a work function of $\Theta = 5.3\,\text{eV}$ [34] and thus $243\,\text{nm}$ photons should not be inducing a photoelectric effect. However, impurities and an imperfect surface structure can considerable reduce the work function in practice. If this proves to be a problem, the gold layer may also be coated with a platinum layer. Platinum offers $\Theta = 5.6\,\text{eV}$[17]. Since platinum has a five times higher electrical resistivity than gold it would be feasible to apply a layer just thick enough to reliable shield the gold coating from UV light and thus retain the conducting characteristics of gold[18].

Although we have yet to test the trap at the time of writing we can estimate its trapping parameters thanks to the fact that our trap is identical to a trap that is already in operation. The following table shows the parameters for trapping $^{40}\text{Ca}^+$ in that experiment.

| $^{40}\text{Ca}^+$ parameters | |
|---|---|
| $\Omega_{\text{rf}}$ | $2\pi \cdot 32.3\,\text{MHz}$ |
| $\omega_{\text{rad}}$ | $2\pi \cdot 3.5\,\text{MHz}$ |
| $\omega_{\text{ax}}$ | $2\pi \cdot 1\,\text{MHz}$ |
| $U_{\text{rf}}$ | $1000\,\text{V}$ |
| $U_{\text{cap}}$ | $1000\,\text{V}$ |

**Table 4.1:** Trapping parameters for $^{40}\text{Ca}^+$ ions at the IQOQI experiment. $\Omega_{\text{rf}}$ is the radio frequency used for driving the trap, $\omega_{\text{rad}}$ and $\omega_{\text{ax}}$ are the radial and the axial trapping frequencies, respectively. $U_{\text{rf}}$ is the voltage of the RF, $U_{\text{cap}}$ is the DC voltage applied to the endcap electrodes. See section 2.2 for the definition of the parameters and the relations between them. Source: M. Guggemos and D. Heinrich, private conversation.

Together with the trap dimensions of $r_0 = 0.57\,\text{mm}$ and $z_0 = 2.25\,\text{mm}$ we can calculate parameters that should be suitable for trapping $^{88}\text{Sr}^+$. With the values given, the stability parameter as defined in equation 2.15 is calculated to be $q = 0.36$ and thus lies as expected in the stable regime. The geometry factor $\alpha$ can be derived from equation 2.20 to be $\alpha = 0.041$.

[17] This number is only valid for a polycrystalline platinum layer. Other platinum structures offer different values (higher and lower) but all of them have $\Theta \geq 5.1\,\text{eV}$

[18] The skin depth of good conducting materials is given by $\delta = \sqrt{\frac{2\rho}{\omega\mu}}$, with resistivity $\rho$, angular frequency $\omega$ of the RF voltage and the absolute magnetic permeability $\mu$ [36]. For an RF field with a frequency of $\omega = 2\pi \cdot 28\,\text{MHz}$, the skin depth is $\delta = 64\,\mu\text{m}$ in titanium, $\delta = 33\,\mu\text{m}$ in platinum, and $15\,\mu\text{m}$ in gold. The thickness of a layer of platinum strong enough to shield the gold plating from UV light would be in the range of a few hundred nm and thus much thinner than the skin depth, meaning that the majority of the RF current would flow in the gold layer.

Applying identical values for $U_{\text{rf}}$ and $U_{\text{cap}}$ to our trap (the values for $z_0$ and $r_0$ stay the same since the trap design is identical) and working with a stability parameter of $q = 0.35$ the following frequency parameters can be derived for trapping $^{88}\text{Sr}^+$ ions:

| $^{88}\text{Sr}^+$ parameters | |
|---|---|
| $\Omega_{\text{rf}}$ | $2\pi \cdot 22.1\,\text{MHz}$ |
| $\omega_{\text{rad}}$ | $2\pi \cdot 2.7\,\text{MHz}$ |
| $\omega_{\text{ax}}$ | $2\pi \cdot 0.67\,\text{MHz}$ |

**Table 4.2:** Expected trapping parameters for $^{88}\text{Sr}^+$ ions at $q = 0.35$, $U_{\text{rf}} = 1000\,\text{V}$, and $U_{\text{cap}} = 1000\,\text{V}$. The helical resonator is designed to have the resonance frequency $\Omega_{\text{rf}} = 2\pi \cdot 22.1\,\text{MHz}$. Trapping with these parameters will be tested in the near future.

The strontium for the experiment is supplied by two commercial ovens[19] that will provide a beam of neutral Sr atoms. These ovens consist of a stainless steel tube that is filled with an alloy containing strontium. It is sealed with indium under a pure argon atmosphere to avoid contamination. To obtain Sr the ovens are heated by a current. Figure 4.16 shows a schematic of the oven.

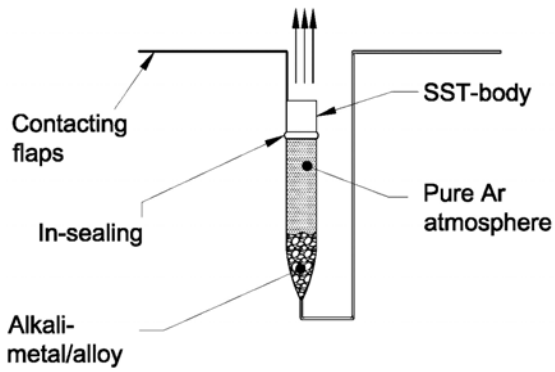


**Figure 4.16:** Schematic image of the strontium source. The diameter of the stainless steel tube is 3 mm and the ovens each contain 50 mg of strontium [37].

As explained earlier, the two ovens are placed inside the hollow post of the titanium trap mount (see figure 4.15) with the help of an oven mount made out of Macor (in this case the good thermal isolation provided by this material is very useful). The Macor piece is designed to align the ovens in such a way that the emitted atomic beams cross the trap center. To reduce the deposition of scattered Sr atoms onto the blades, an aperture is located between the ovens and the trap. This aperture consists of a small slit cut in the frame of the trap mount right under the sapphire holder, see figure 4.15. Figure 4.17 shows a picture the oven holder, while appendix A shows the design in more detail.

[19] Alvasource Sr-50V bought from Alvatec, see [37] for further information on this product.

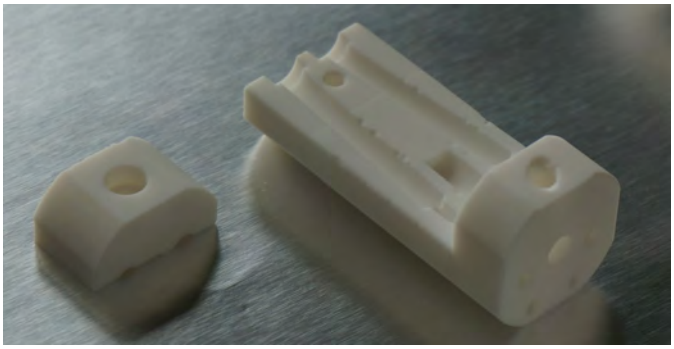

**Figure 4.17:** Holder for the strontium sources. The mount is made out of Macor and aligns two ovens to emit the atomic beams into the center of the trap. Each oven can be separately switched on and off. Note that the Macor piece on the left side of the picture was intended to fixate the ovens. However, it proved to be interfering during the assembly process and thus was replaced by two washers.

## 4.3 Vacuum chamber

The main element of our vacuum setup is the chamber housing the ion trap. It is a six inch spherical octagon[20] which provides two DN100CF and eight DN40CF ports while being quite compact ($177.3\,\text{mm} \times 177.3\,\text{mm} \times 70.6\,\text{mm}, 5.16\,\text{kg}$). Our trap offers three different optical axes: through the endcap electrodes along the ion chain, perpendicular to the ion chain in the horizontal plane and at an angle to the ion chain in the vertical plane. The trap is placed inside the chamber in such a way that we have access to all three optical axes. Thus, six ports are reserved for viewports while the other four ports can be used for feedthroughs and vacuum pumps. Figure 4.18 shows the schematic of the setup, figure 4.19 is a corresponding photograph. The three optical axes are used as follows:

1. Axis I goes through the holes drilled in the endcap electrodes. It coincides with the axial direction of the trapping potential so that light shining along this axis has a maximal momentum transfer to the axial center-of-mass motion of the trapped ions. Thus, from this direction the largest Lamb Dicke parameters and highest Rabi frequencies are achieved. Laser light which is sent into the trap along this path interacts with all ions inside the trapping region. We use this axis to shine photoionisation light into the trap because it is orthogonal to the axis along which the atomic strontium beams enter the trap. Thus, the Doppler effect in this direction is small. Besides ionisation the feature of addressing the entire ion chain at once opens further possibilities, including global qubit manipulation, state initialisation, and sideband cooling with $674\,\text{nm}$ light.

2. The second optical axis (II) is aligned to go diagonally through the trap. We use this direction for laser cooling (Doppler cooling and sideband cooling) and repumping with wavelengths of $422\,\text{nm}$, $1033\,\text{nm}$, and $1092\,\text{nm}$, respectively. The main reason for using this axis for the cooling is that the beams go through the

[20] MCF600-SphOct-F2C8, 316L stainless steel from Kimball Physics

trap at an angle such that the photon momentum has a projection onto all three trap axes. This makes it possible to cool modes in all three dimensions with light coming from only one direction. Note that one port of this axis in combination with a Tee connector also provides a joint for connecting a turbo pump.

3. The third optical axis (III) is perpendicular to the ion chain and passes through the DN100CF ports of the chamber. This direction has the best optical access which can be used with high-NA optics for efficient fluorescence detection. Thus we will use this direction for fluorescence detection of ions via scattered 422 nm photons on an EMCCD camera[21]. This direction also allows us to address individual ions in the chain. Since we want to be able to do qubit manipulation and Rydberg excitation of individual ions we will use this axis for shining 243 nm, 305 nm – 310 nm and 674 nm light into the trap. The focal length of the addressing lens is not the same for the UV wavelengths, 422 nm, and 674 nm light and the standard anti-reflection (AR) coating for the lenses does not cover both wavelength regions. Thus, we will send in UV laser light from one side and at the other side we will send in 674 nm laser light and collect 422 nm fluorescence.

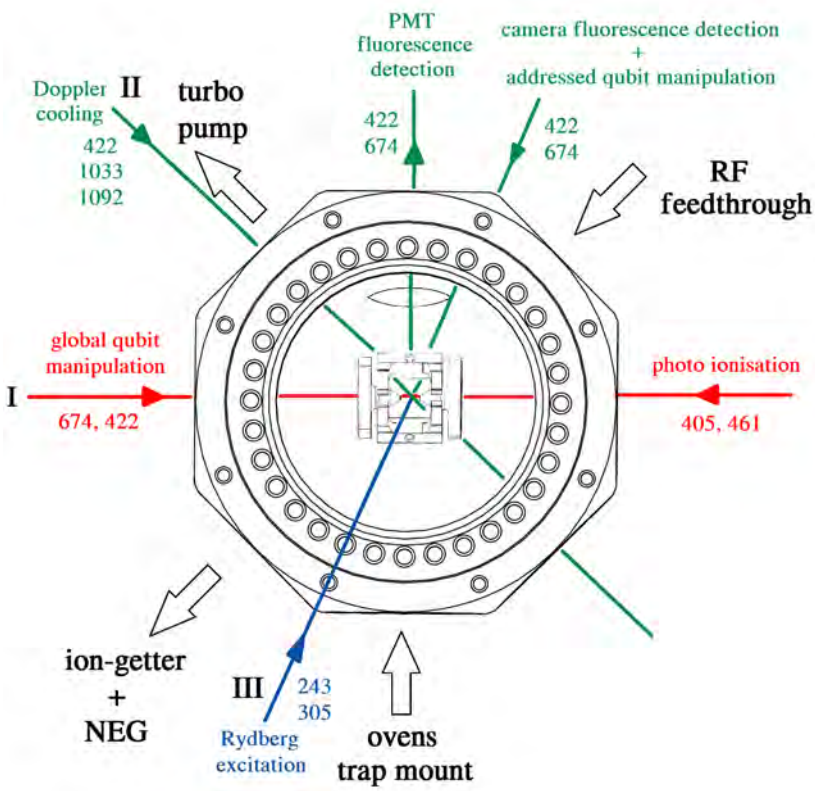


**Figure 4.18:** Schematic of the vacuum chamber. There are three optical axes marked with I (red), II (green), and III (blue plus green, front to back). The colours for the beams coincide with the colours used for the transitions in the level scheme in figure 4.1. A lens for collecting light for the PMT is mounted above the trap inside the chamber.

[21] Andor iXon3 897, type A-DU897-DCS-BBB

Beside these three axes we have additional optical access to the trap through a hole in the titanium trap mount. We plan using this access to look onto the trapping center through an aspherical lens. This lens is fixed inside the vacuum chamber and thus cannot be moved to adjust the focus or tilt. Due to that it is not yet clear how well one can image the trapped ions through this system.

For optical access into the vacuum chamber we use two different sets of viewports. One set[22] is AR-coated for 422 nm, 1033 nm, and 1092 nm and is used on axis II. The other set of viewports is more complicated due to their anti-reflection coating requirements. As already stated we intend to use four different wavelengths along the axis perpendicular to the ion string, namely 243 nm, 305 nm, 422 nm, and 674 nm. Although we use the UV light and the other two wavelengths from opposite directions it is important that the AR-coating of both windows is optimised for all four wavelengths to reduce reflections from light leaving the chamber. This is especially true in the UV regime, since photons reflected onto the trap may cause charging of the surfaces due to the photoelectric effect. We also want to keep the possibility open to test global Rydberg excitation. We therefore use viewports with the four wavelength AR-coating for axes I and III.

**Figure 4.19:** Assembled chamber prior to the vacuum bake. The orientation is the same as in the schematics in figure 4.18. The valve for connecting the chamber to an external pump is mounted on the upper left flange of the octagon, the RF feedthrough on the upper right flange and the tube for connecting the combined ion getter and NEG pump on the lower left flange, respectively. On the bottom is the conical reducer and the electrical feedthrough. For the high temperature vacuum bake the chamber was sealed with blind flanges.

[22]These viewports were manufactured by VACOM.

It is not easy to engineer AR-coatings for this wide range of wavelengths and only one company[23] offered satisfying reflectivities. However, their manufacturing process for this coating limited the viewport size to DN40CF. So for the two DN100CF ports we reduced the diameter to DN40CF. Such reducers are widely available but typically have a thickness of 20 mm. In our case such an additional distance between trap and window has to be kept at around 10 mm because the addressing lenses mounted outside the chamber must be 73 mm from the trap center for imaging and focussing the laser beams down onto the ions. I therefore designed a thinner reducer[24] to overcome this problem.

Three ports are used for vacuum pumps and electrical feedthroughs as shown in figure 4.19. The vacuum pump is a combined system of an ion pump and a non-evaporative getter (NEG) pump[25]. Since the ion pump works with a magnetic field it has to be kept at a sufficient distance from the ion trap. After consultation with the company we decided to add an additional tube with a length of 70 mm between the chamber and the pump so that the distance between the ion pump and the trap is around 160 mm. This decreases the effective pumping speed but renders the magnetic field of the pump in the center of the trap negligible, see appendix C for further details. The final open port is used to mount the ion trap and to feed through wires that connect to the endcap electrodes, the compensation electrodes and the strontium ovens. Since it is not possible to get enough feedthroughs capable of handling the required currents and voltages on a DN40CF flange, we use a DN63CF flange in combination with a conical reducer.

## 4.4 Addressing lens

The lenses used for fluorescence imaging and addressing trapped ions individually with the qubit manipulation light and the UV light for Rydberg excitation are aspherical lenses[26] with diameters of 50 mm, effective focal lengths of 80 mm at the design wavelength of 285 nm and a numerical aperture of 0.29. They will be positioned outside the vacuum chamber at a distance[27] of around 73 mm from the center of the ion trap, the exact distance depends on the laser wavelength. Table 4.3 shows the simulated values for the wavelengths of all four lasers that pass these lenses in our setup. Figure 4.20 shows a simulation of a lens focusing light through the glass of the viewport. All simulations are done in Zemax.

[23] CCFE - Culham Centre for Fusion Energy, United Kingdom Atomic Energy Authority, UK
[24] This custom reducer was machined by VACOM, the detailed layout is shown in appendix B.
[25] Saesgetters NEXTorr D 100-5
[26] Asphericon 50-80-FPX-S with coating UV (for 243 nm and 305 nm) and A2 (for 422 nm and 674 nm).
[27] The distance is measured between the optical surface of the lens facing the trap and the center of the trap.

| $\lambda$ [nm] | BFD [mm] |
|---|---|
| 243 | 68.8 |
| 305 | 72.6 |
| 310 | 72.8 |
| 422 | 75.6 |
| 674 | 77.7 |

**Table 4.3:** Simulated back focal distance (BFD, distance between the last optical surface of the lens and the focal point) of the aspherical 50 mm lens for the different wavelengths used in our setup. These values include a 3 mm thick window made out of fused silica between the lens and the focal point.

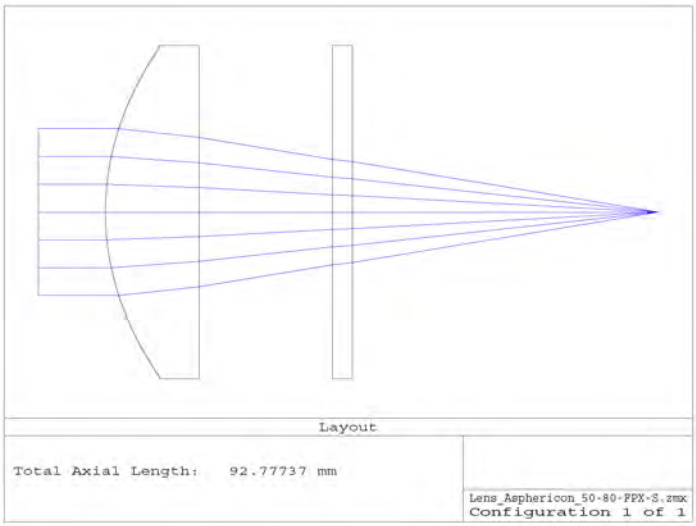


**Figure 4.20:** Simulation of the 50 mm aspherical lens used for individual addressing of trapped ions. The lenses are made out of fused silica and are anti-reflection coated corresponding to the respective wavelengths.

Simulations show that with these lenses it should be nearly possible to achieve a diffraction-limited focus with an Airy radius of around 1.3 $\mu$m for both the 243 nm and the 310 nm light of the Rydberg excitation lasers. For the qubit transition at 674 nm, an Airy-radius of about 1.6 $\mu$m is predicted. At this wavelength we are not in the diffraction-limited regime any more, most likely due to aberrations. The simulations give us a root mean square (RMS) radius of 4.1 $\mu$m when the whole lens is illuminated and show a decreasing RMS radius as the aperture size decreases. Since the typical distance of ions trapped in a linear Paul trap is roughly 5 $\mu$m, individual addressing with all three wavelengths should be possible with our system. Figure 4.21 (a) shows the simulated spot diagram for 310 nm light. In figure 4.21 (b) the fraction of beam energy enclosed in a circle is plotted against the circles radius. The simulations show that at the focus the beam should be nearly diffraction limited.

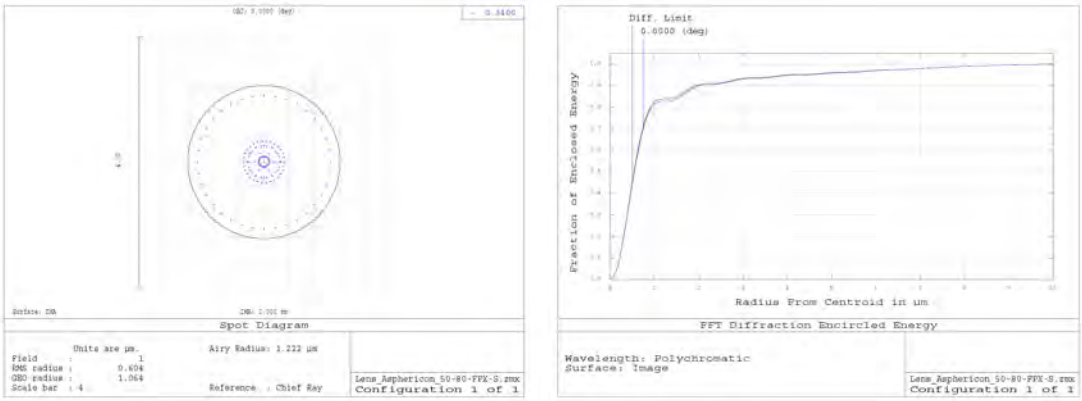


(a) (b)

**Figure 4.21:** Simulation of the spot diagram (a) and the enclosed energy (b) for the addressing lens at a wavelength of 310 nm. The simulated rays in the spot diagram lie well within the diffraction-limited Airy radius of 1.2 $\mu$m for an input aperture of 25 mm. The simulated performance of the lens in this configuration is nearly diffraction limited and should be suitable for addressing of individual ions inside the trap separated by approximately 5 $\mu$m.

We will also use these lenses for imaging the ions with scattered 422 nm fluorescence light and therefore have measured and calculated the modulation transfer function (MTF) of the lens at this wavelength. The MTF is used to describe the contrast (or modulation) of an image, meaning how well patterns of different periodicities (for example lines with different distances in between) can be resolved by an imaging system [38]. The modulation (i. e. visibility) is given by

$$\text{modulation} = \frac{\max - \min}{\max + \min} \quad , \tag{4.2}$$

where max and min are the maximal and minimal brightness of the lines and the space in between, respectively. Since the modulation is dependent on the resolution of the optical system, it is linked to the distance between the lines being imaged. Thus, the MTF is a function of the spatial frequency, where the spatial frequency $v$ is given by the number of lines per unit length[28] in the object. The modulation transfer function then takes the form

$$\text{MTF}\,(v) = \frac{\text{M}\,(v)}{\text{M}\,(0)} \quad , \tag{4.3}$$

where $\text{M}(v)$ is the modulation of a pattern with spatial frequency $v$. $\text{M}(0)$ is the modulation of the overall background of the image, taking into account the illumination of the whole setup. In the following few paragraphs we measure the MTF and the imaging resolution of our addressing lens and compare it with the simulations done in Zemax.

[28] In optics it is common to speak of this spatial frequency $v$ as "cycles per mm". One cycle consists of one bright and one dark line of the pattern.

To test the MTF of our imaging system a resolution test target[29] serves as an object. It is illuminated by white light filtered with a bandpass filter[30] which gives blue light with wavelengths between $422$ nm and $435$ nm. The target is illuminated with the Köhler illumination technique in such a way that the target is equally bright across and at the same time the whole aperture of the $50$ mm aspherical lens which collects the light is illuminated. Finally, an achromatic lens[31] focuses the light onto the CMOS chip of a camera[32]. Figure 4.22 shows the camera image of the target.

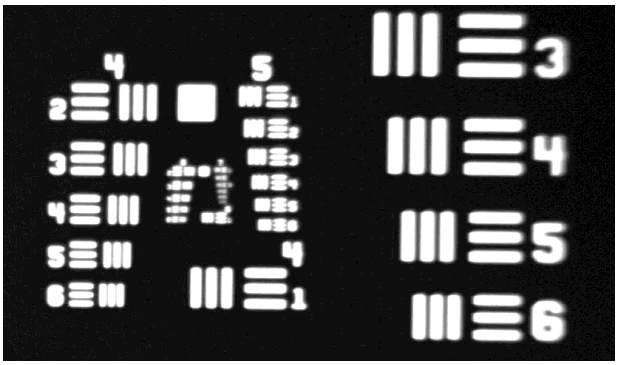

**Figure 4.22:** Image of the resolution test chart used for the resolution measurement. The target offers test patterns with spatial frequencies of up to 228 cycles per mm. The regime of single digit $\mu$m resolution starts at $v = 50$ cycles per mm or the fifth pattern from group number five. Please note that the image was digitally altered from the original greyscale image for printing purposes.

We evaluate the greyscale values of vertical pixel rows which contain patterns of the groups with number four, five and six (the seventh group is not resolved any more). Figure 4.23 shows the resulting graphs for the fourth and the sixth group. From these graphs we calculate the modulation of each pattern according to equation 4.2 as well as the overall background modulation $\mathrm{M}(0)$. We derive the resulting MTF according to equation 4.3 and plot it. Figure 4.23 shows the measured modulation transfer function (red curve) together with the simulated MTF for this setup (blue curve, Zemax data) and the simulated diffraction limited resolution (black curve, Zemax data). The simulated and measured results coincide quite well with each other. The data shows that patterns with intermediate distances of $4.3\,\mu$m can be resolved with a modulation of around $0.1$. The green curve is from a Zemax simulation with illumination by $422$ nm light.

Note that the setup is still far from ideal when one compares the result to the diffraction-limited curve. Simulations show that the resolution should improve significantly if the wavelength of the light is more narrow. Since the bandwidth of the light was with $15$ nm quite broad we expect a significant improvement in resolution for scattered $422$ nm laser light.

[29] Negative 1951 USAF test target from Thorlabs
[30] Semrock Filter SEM-FF01-427/10-25
[31] Thorlabs AC508-300-A
[32] Sony NEX-6

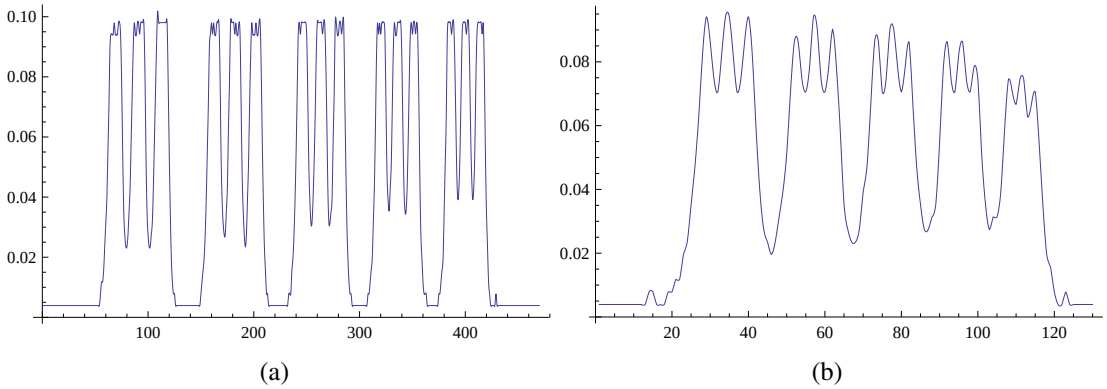


**Figure 4.23:** Line graphs from the original greyscale image shown in figure 4.22. The position of the pixel in the selected row (x-axis) is plotted against its greyscale value (y-axis). Graph (a) shows the intensity values for the patterns two to six of group number four from the test target. One can clearly see the minima and the maxima of the different sections. Graph (b) shows the data for the sixth group, again for pattern two to six. The patterns were still resolved although the modulations declined. In the six pattern of this group (rightmost in the graph) the distance between two lines is $4.4\,\mu$m. This was resolved with a modulation of $0.1$

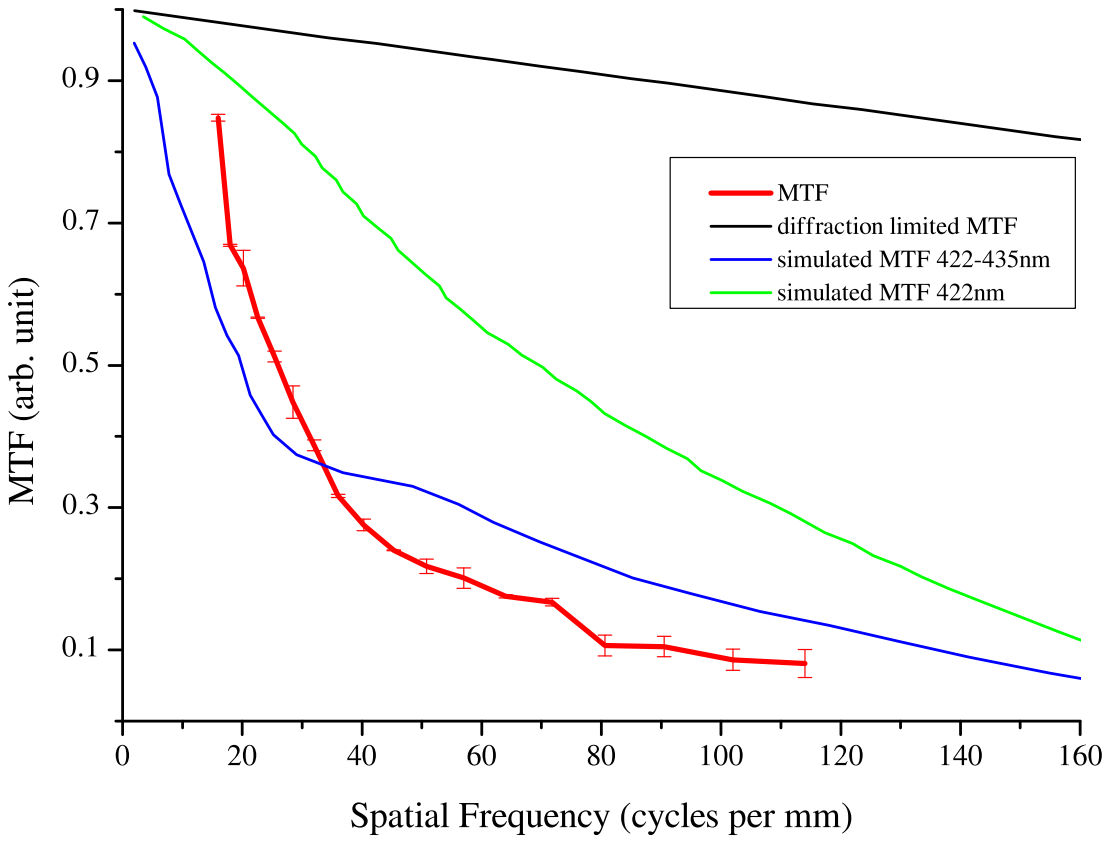


**Figure 4.24:** Comparison of measured MTF (red curve), the simulated MTF (blue curve) and the simulated diffraction limited MTF (black curve) of the imaging setup. Simulations show a better resolution for the scattered $422\,\text{nm}$ light (green curve) than for scattered $422\,\text{nm} - 435\,\text{nm}$ light.

## 4.5 Assembly of the setup

This section describes the assembling process of the ion trap and the vacuum chamber along with the applied cleaning and bake-out procedures. The vacuum chamber was first partially put together without the trap to perform a vacuum bake. Then, in order to mount the trap inside the vacuum chamber the setup had to be completely disassembled again. Thus the description of the assembling process is structured in chronological order: cleaning and bake-out procedure, assembly of the trap and assembly of the chamber. A very good introduction into handling ultra-high vacuum (UHV) systems can be found in [39].

### 4.5.1 Cleaning and bake-out process

When working with an UHV setup it is crucial to thoroughly clean and carefully handle and store every surface inside the vacuum chamber. Naturally, it is also necessary to prepare the workplace and all tools accordingly. Cleaning of all pieces was performed in an ultrasonic bath. Our cleaning process consisted of three main steps which are described below.

1. Ultrasonic cleaning of all parts in normal tab water mixed with soap[33]. This step removes all kinds of dirt and grease remaining on the parts due to machining processes and general handling of the items. The parts were placed in the bath for around 20 minutes and then rinsed with fresh water to remove residues from the soap. Since this was the first step in our cleaning process we used tab water for rinsing.

2. The next step consisted of ultrasonic cleaning in an acetone[34] bath, again for around 20 minutes. Aceton is a very good solvent for grease and oils and thus should reliably remove any traces left of these substances. We rinsed the parts with fresh acetone after taking them out of the bath. After this cleaning step, one must not touch the items without gloves or bring them in contact with something that is not perfectly clean. Thus, the parts were stored on UHV-compatible aluminium foil[35] or similar clean materials like lint-free tissues[36] suitable for clean room environments. Additionally, to prevent the parts from getting dusty, everything was again covered with UHV foil.

3. In the last cleaning step we put the parts in an ultrasonic bath of methanol[37] to remove any residue from the acetone. Since inhaling methanol is harmful and it evaporates rapidly in the warm environment of the ultrasonic bath, this step had to be done under an activated exhaust (this was also the case for the acetone bath). We left the parts in the bath for around 10 minutes. After taking a piece out of the bath it was again rinsed with fresh methanol and left under the exhaust for drying.

[33] Tickopur R33
[34] GPR Rectapure acetone, purity at least 99.5%
[35] All-foils, inc. UHV foil
[36] VWR Spec-Wipe 3
[37] GPR Rectapure methanol, purity at least 99.5%

Every item of the UHV setup was cleaned according to this process. We also prepared the tools for assemble the UHV setup that way. For tools with parts that are affected by acetone (like plastic handles) step two was carried out with isopropyl alcohol[38]. The screws were partially delivered already cleaned. Those which were not clean and were not used inside the chamber but outside for closing flanges etc. were cleaned up to step two. This is not strictly necessary but lowers the risk of accidental contamination during assembly.

When working with vacuum, even if everything has been cleaned perfectly, one has to worry about the outgassing rates of the different materials [40]. Outgassing is the release of gases like hydrogen, water, oxygen, nitrogen and carbon dioxides that were adsorbed on the surface or trapped inside the materials, but also the evaporation of the material itself. Good materials for UHV are, for example, stainless steel, aluminium, gold, titanium, Macor, sapphire and glass. The first limitation for the vacuum is usually water adsorbed on the surface which can be removed through moderate baking with temperatures above $100\,^{\circ}$C. Once the UHV region is reached, the main concern for materials like stainless steel is the outgassing of hydrogen which was trapped inside the bulk during the production process. The outgassing rate of hydrogen increases exponentially with the temperature since the diffusion rate in the material increases. Thus a baking of the parts used in an UHV setup helps to deplete the amount of gases trapped inside the material. For stainless steel, bake-out temperatures higher than $300\,^{\circ}$C are usually employed to efficiently release the hydrogen from the material. Higher temperatures will speed up the process. A good description of this topic can be found in [41]. There are two different types of bake-outs, the air bake and the vacuum bake. In an air bake the parts are baked out under a normal atmosphere. In the case of stainless steel the air bake will also form a layer of iron oxide and chrome oxide on the surface [40]. This oxide layer has a very low permeability for hydrogen and thus reduces the diffusion of hydrogen from the bulk to the surface and inhibits the re-absorption of hydrogen once the bake is finished. An air bake can be done with the unassembled setup. Higher temperatures are possible since there is no risk of damage due to stress between parts made of different materials. It is also easier to omit delicate pieces like viewports which could be damaged in this temperature regime. An air bake is often followed by a vacuum bake of the assembled system. In a vacuum bake the diffusion rate of hydrogen in the bulk is increased. Once a hydrogen atom reaches the surface, it can react with other hydrogen atoms to $H_2$ gas which is pumped away. A vacuum bake can be either done in a special oven where the oven chamber can be set under vacuum or with the assembled vacuum chamber being pumped and heated at the same time. The latter is done in our case. In a vacuum bake-out one does not need to worry about harmful oxidation of, for example, electrical connections made of copper. Another difference compared to an air bake is the fact that whatever evaporates from the surface during the bake is pumped away. Thus, one not only removes hydrogen from the bulk matter but also remaining substances on the chamber walls like water vapour or residues from the cleaning solvents. For baking, we have access to an industrial oven at our institute. This oven is large enough to house

[38] GPR Rectapure 2-propanol, purity at least 99%

our assembled vacuum chamber as a whole. Through a duct cut in the oven's wall the chamber inside the oven can be connected with a vacuum pump station located next to the oven. Thus, it is possible to bake the chamber while pumping it at the same time.

The ion trap and the vacuum chamber are mainly made from steel, aluminium, titanium and sapphire. Steel and aluminium have significantly higher outgassing rates than titanium and sapphire. We therefore first performed an air bake of all steel and aluminium parts (the chamber, blind-flanges, tubes, connections and the lens holder tube). For this, we heated the oven up to $450\,°$C with a slope of $60\,°$C/h, let the parts soak at this temperature for 8 hours and then ramped it back down to room temperature using the same slope. Figure 4.25 shows the parts directly after the air-bake. After that, the basic vacuum setup was assembled and prepared for a more gentle vacuum bake. In order to bake all the parts that are used inside the vacuum chamber (connections and all trap parts except the sapphire pieces), we staked them into the chamber piece by piece before the vacuum bake. Copper forms a brittle oxide layer at high temperatures and thus all flanges containing electrical and RF-feedthroughs were not air baked. For the vacuum bake they were incorporated in the setup, since the vacuum side does not oxide during the vacuum bake. The oxide layers on the air side were removed later.

**Figure 4.25:** Photograph of the parts that were air baked. In the upper right corner one can see the vacuum chamber, in the upper left corner the conical reducer. The two metal plates in the front are the custom-made DN100CF to DN40CF reducers.

It is also very important to keep in mind that cold welding can become an issue between very clean and smooth metal surfaces. If the surfaces are forced together, cold welding can easily happen at room temperature, but even more when the setup is heated [42, 43]. Especially cleaned screws are prone to cold weld with threaded holes or nuts. While this is very annoying but usually repairable when it happens to a connection held by a screw and a nut in a plain hole, it is devastating when a screw gets stuck in a threaded hole since it cannot be removed without destroying the thread. To make sure that no screw gets stuck in the chamber, all of these screws were silver plated. The thin silver layer loosens if the screw is undone, thus preventing cold welding. After pumping down the chamber and performing a helium leak test we started the vacuum bake. The chamber was slowly ($15\,°$C/h) heated to $300\,°$C and kept at this temperature for $300$ hours before ramping down at the same speed. The pressure after the vacuum bake was $2.6 \cdot 10^{-9}$ mbar which corresponds to the pressure limit people usually observe for this

pump station[39]. We could not immediately start assembling the trap and thus flooded the chamber with argon to prevent air from leaking inside.

### 4.5.2 Assembly of the vacuum setup

The assembling process of the setup after the vacuum bake consisted of three major steps. First, the ion trap was built and mounted in the titanium holder. Then the whole assembly was fixed in the vacuum chamber. The second step was to place the strontium ovens in the Macor mount and to connect them with the electrical feedthrough. The ovens were positioned and the endcap and compensation electrodes of the trap were connected. In the last step the aspherical lens was mounted and the chamber was closed. The following subsection describes the assembly process in detail.

The ion trap was assembled as follows: first the four blade electrodes were screwed to the central piece of sapphire, see figure 4.26 (a) for the result. Next the endcap electrodes were put into place using two additional sapphire parts. The completed trap was then mounted into the titanium holder and the compensation electrodes were pushed into their respective position. One electrode was gold plated (see figure 4.14 (d)) because it is positioned close to the beam path of UV light. However, that additional layer made it too thick to fit through the drillings. After carefully lifting of the gold layer it could be put in place (the uncoated compensation electrode fit without any problem). Finally, the endcap electrodes were connected to stainless steel wires while the blade electrodes were connected to especially made wires cut out of thin copper plates. The result is shown in figure 4.26 (b). After that, the trap was ready to be set inside the vacuum chamber. To mount the holder in place we used a "groove grabber"[40]. It consists of two stainless steel pieces that are clamped into the grooves on the inside of the chamber's flanges. The lower part of the titanium mount was designed to fit into such a holder.

After mounting the trap inside the chamber we assembled and connected the strontium ovens. Both ovens were placed into the Macor holder and connected with Kapton-insulated copper wires. The connection between oven and wire was done through folding and clamping the oven's stainless steel stripes before and after the tube, see figure 4.27 (a). This saves space compared to using clamps (soldering does not work since the ovens are heated to evaporate the strontium inside). The Macor piece originally designed along with the holder to retain the ovens could not be used as intended. It tilted when we tried to push the mount inside the titanium handle and thus had to be removed. Although the wire is 1 mm thick, thus sturdy and by itself keeps the oven firmly in place, we didn't want to take any risks of misalignment. The original mount was therefore replaced with two washers, see figure 4.27 (b). Although this connection now is far more thermally conducting than the original mount we expect that we are still able to switch the ovens on and off individually.

[39]The turbomolecular pump in use is a Leybold Heraeus TURBOVAC 600 with a compression ratio for $N_2 > 10^9$. The ultimate pressure stated by the manufacturer is $< 10^{-10}$ mbar.
[40]Kimball Physics, product number MCF275-GrvGrb-CYL1000

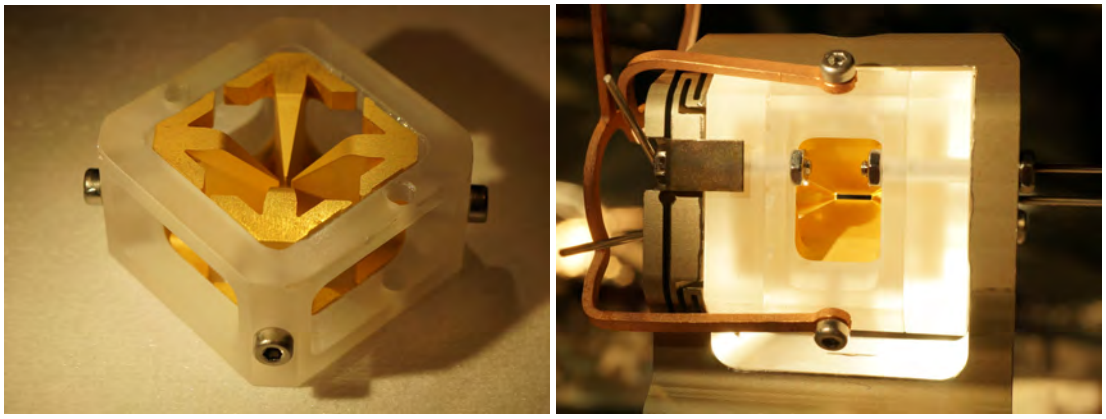

(a) (b)

**Figure 4.26:** Pictures of the partially (a) and the completely assembled trap (b). In (a) the blade electrodes are mounted in the central sapphire piece. The screws used to lock the blades in position in this step are later on replaced by slightly longer ones. In (b) the trap is completely assembled and the sapphire mount is placed into the titanium holder. The sapphire is fixed with four screws to the holder, two on each side of the trap. The copper wires for the radio frequency are connected to the blade electrodes with the now longer set of screws. On each side of the trap the stainless steel connections for the endcap electrodes and the compensation electrodes can be seen. The left side of the titanium holder is cut to form a spring. This should reduce stress on the sapphire mount in case of temperature changes in the system.

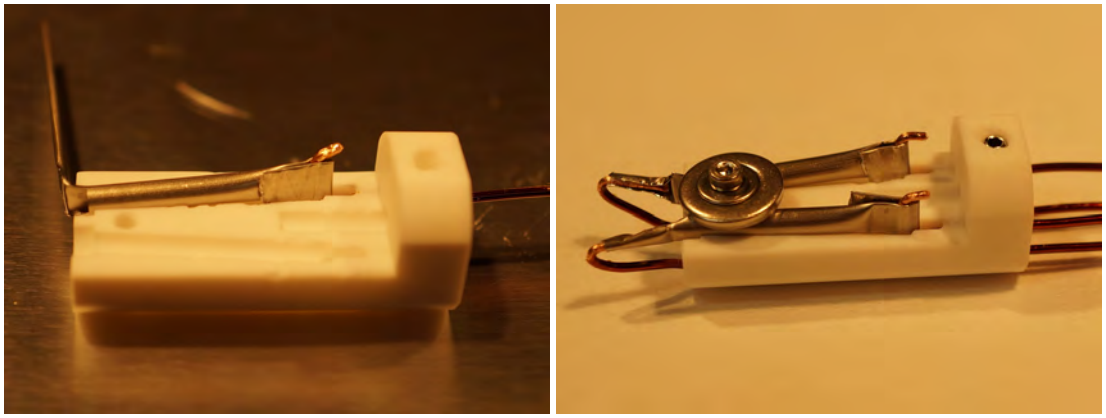

(a) (b)

**Figure 4.27:** Assembling process of the ovens. Picture (a) shows the Macor holder with one partially connected oven. While the lower part of the oven is already folded and clamped to the copper wire, the upper metal stripe still has its original form. In picture (b) the assembly is completed, both ovens are connected and fixated with washers. The alignment of the ovens is slightly tilted so that the atomic beams cross $43.5$ mm above the holder. In the end the oven mount is positioned inside the titanium holder in such a way that the crossing point coincides with the center of the trap.

To install the oven holder inside the trap mount, it is clamped to a stainless steel rod with a diameter of 3 mm which is screwed into a threaded bore in the middle of the electrical feedthrough. A set screw in the base of the Macor holder enables us to adjust the height of the holder on the rod and thus the position of the ovens inside the titanium holder such that the emitted atom beams cross in the center of the trap. The Kapton insulated copper wires from the oven are connected to the wires from the feedthrough with barrel clamps. The feedthrough wires are bare so we insulate them with ceramic pearls to avoid any shorts. See figure 4.28 (a) for the setup so far.

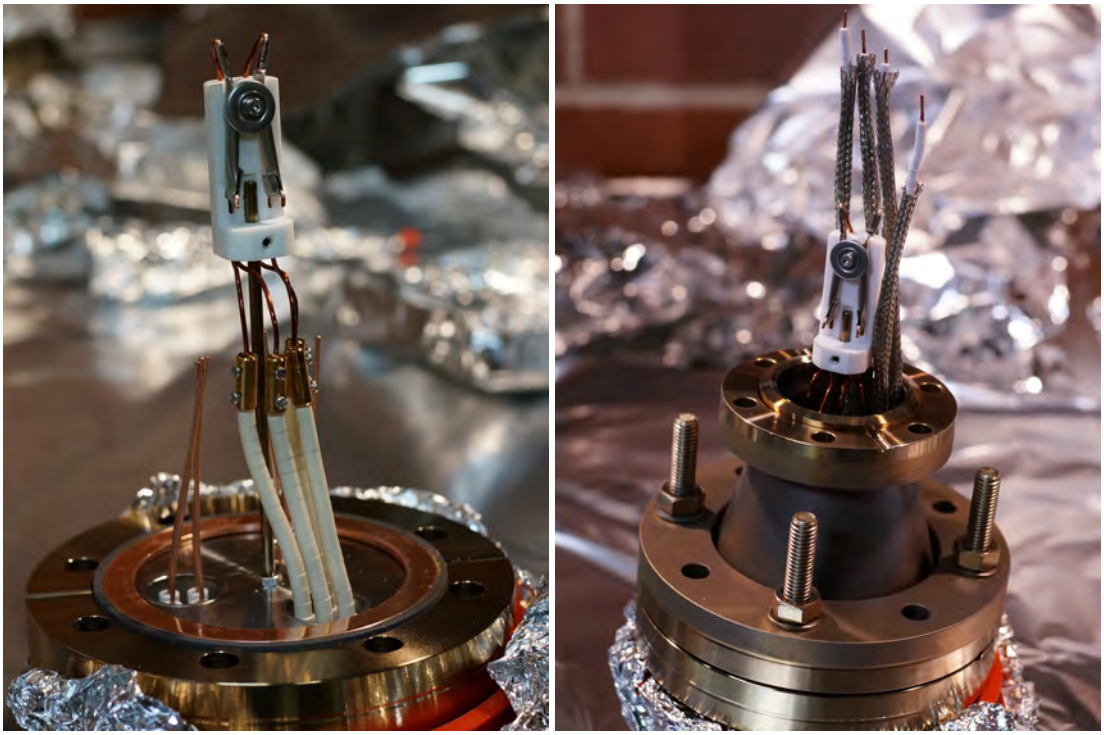

(a) (b)

**Figure 4.28:** The oven holder is clamped to a stainless steel rod that keeps it in the right position. The ovens are then connected to the wires from the feedthrough, see picture (a). The next step is to prepare the connections for the endcap and the compensation electrodes. These wires are covered with a stainless steel mesh to provide shielding from RF-fields. Picture (b) shows the setup with the conical reducer already in place, ready for being attached to the chamber.

As already stated before, the endcap and the compensation electrodes are connected to the same feedthrough. The copper wires from the feedthough were extended with pieces of Kapton insulated wire to the required length. To prevent any shorts due to a harmed Kapton insulation not only the bare wires but also the insulated wires were threaded with ceramic pearls. An additionally stainless steel mesh around the wires shields electromagnetic interference. In the next step the conical reducer was set onto the feedthrough, see figure 4.28 (b), and the whole assembly was carefully put into place. After connecting the endcap and the compensation electrodes to the respective wires, all contacts were carefully tested for connectivity and shorts.

The next step in the assembly process was to put the aspherical imaging lens inside the chamber and to adjust the focus on the trap center. The lens with a diameter of one inch is mounted with a custom-made holder machined by the mechanical workshop at our institute. It consists of a threaded aluminium tube and an round retainer cap. The lens was placed into this cap which is then screwed onto the tube and thus holds the lens in place. Figure 4.29 (a) shows both pieces of the aluminium holder. When fastening the cap one has to be careful not to tighten it too firmly to prevent birefringence due to stress inside the lens. The tube itself was mounted with a groove grabber inside the vacuum chamber, identical to the one holding the titanium mount. To adjust the lens to the right distance from the trapping center the following method was used: with a strong spotlight we shone light onto the blade electrodes. The lens mount was placed inside the chamber but was still loose enough inside the groove grabber so that we were able to move it up and down. The lens then projected an image of the trap electrodes to a plane above the chamber. Moving the aluminium holder and thus the lens up and down one was able to adjust the position of the focal point. The aim was to create an image as sharp as possible at a point as far away from the trap as possible. In our case we ended up with a nice projection of the trap on a sheet of paper stuck to the ceiling of our laboratory. See figure 4.29 (b) for the resulting image.

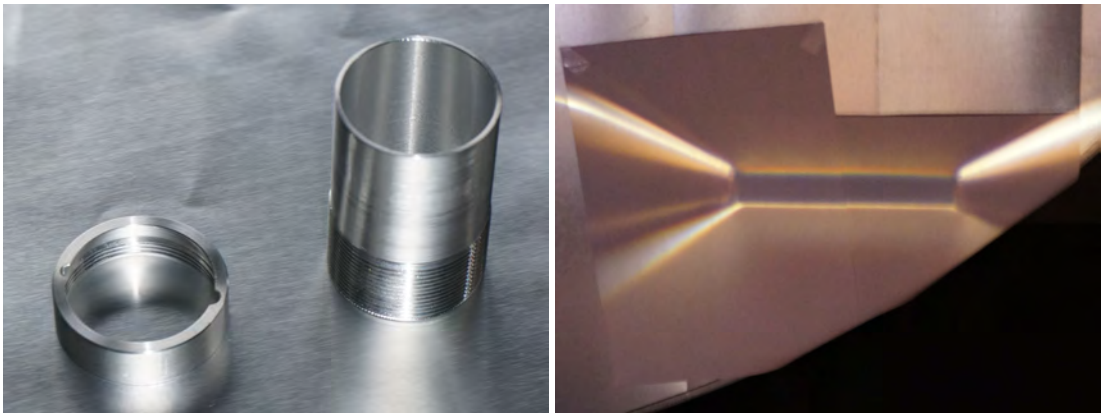

(a) (b)

**Figure 4.29:** Picture (a) shows the aluminium lens holder for mounting an aspherical lens inside vacuum. The lens is placed into the cap on the left hand side and afterwards is screwed onto the tube. The tube itself is slightly conical since the inner diameter of the groove grabber as well as the lens diameter are one inch each. Notches in the rim of the cap prevent creation of virtual leaks between lens and holder. (b) shows the image of the trap through the lens. The endcap electrodes along with the upper pair of blade electrodes can be nicely seen.

Before closing the chamber the RF-feedthrough was installed and connected to the blade electrodes. The photograph in figure 4.30 shows this last stage of the open chamber. The trap is fully connected and the aspherical lens is in place. Before connecting the chamber to the turbo pump we measured the capacitance of the compound trap and RF-wires to be $(11.6 \pm 0.1)$ pF. Also all other electrical connections were tested to

work. The closed chamber was then pumped down for a few days but without being baked. An end-pressure of $2.5 \cdot 10^{-9}$ mbar was reached so after the assembly we were again limited in pressure by the turbomolecular pump system. With the trap inside vacuum, the capacitance changed to around $10\,\mathrm{pF}$ at $100\,\mathrm{kHz}$. Since the viewports from CCFE were not yet delivered[41], the chamber was again flooded with argon and put on its place on the optical table.

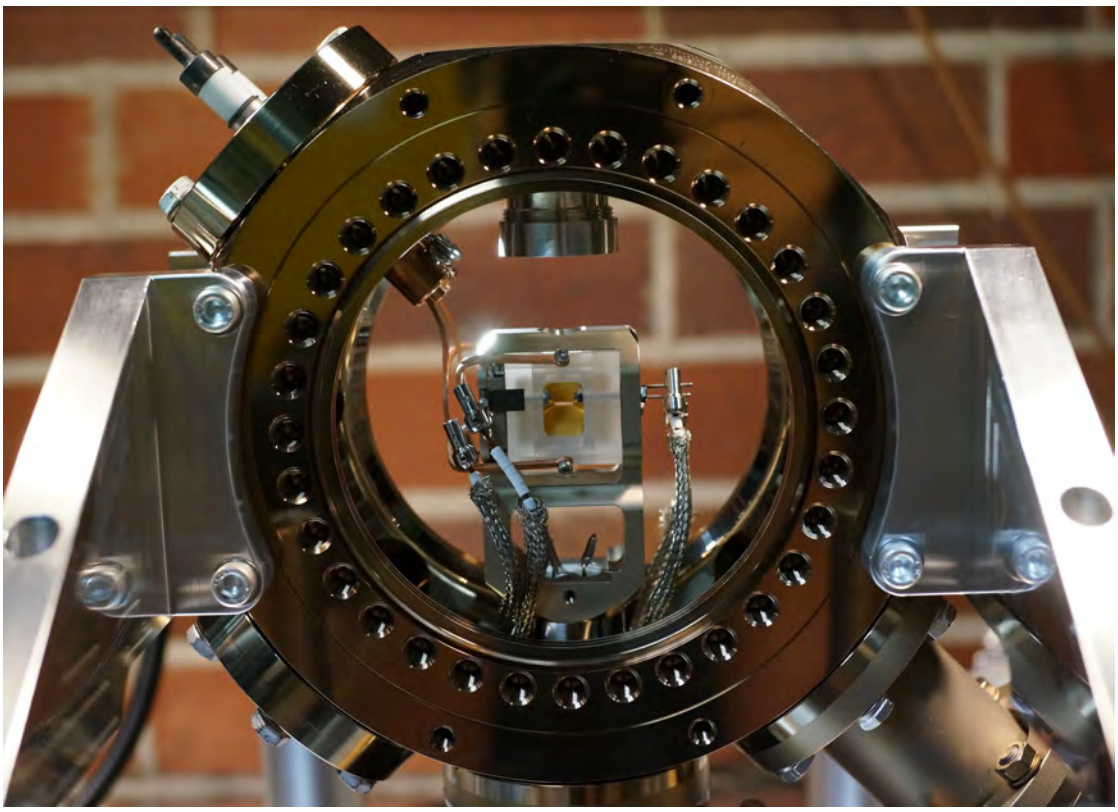

**Figure 4.30:** Vacuum chamber with assembled ion trap. The trap is fully connected to the feedthrough below (DC and compensation electrodes as well as the ovens) and to the RF-feedthrough in the upper left corner (RF electrodes). Directly above the trap the holder containing the aspherical lens can be seen. The chamber was closed after taking this picture.

[41] The first patch of view ports from this company was delivered at the end of September 2013. However, the coating on all the windows was flawed and thus the patch was sent back. A new patch is expected to arrive in march.

# Chapter 5

# Summary and outlook

After working for about one and a half years on setting up our experiment for generating trapped Rydberg ions, the major preparation steps and key components are completed or on the verge of being finished. We started with setting up the laser systems for trapping, cooling and manipulating strontium ions and with the exception of the $674\,\mathrm{nm}$ laser used for sideband cooling and state manipulation, all lasers can now be frequency stabilised. The lasers for photoionisation of strontium atoms as well as the $1033\,\mathrm{nm}$ and the $1092\,\mathrm{nm}$ repumping lasers are fully operational. The $422\,\mathrm{nm}$ laser only requires acousto-optical modulators to tune the laser on resonance of the ionic transition. With this, all lasers will be ready to trap the strontium ions.

The major part of my work in the lab (besides working with the lasers) focused on preparing and assembling the ion trap and the surrounding vacuum chamber, and choosing suitable lenses for single ion addressing and imaging. The trap was designed at the Institute for Quantum Optics and Quantum Information. The design was adapted to allow for better optical access to the trap from above. The main question concerning the addressing lenses was whether they should be placed inside the vacuum chamber or on the outside. Simulations with an optics designing software showed that aspherical lenses placed outside the chamber should be sufficient to focus laser light down to $5\,\mu$m as well as to image individual ions separated by this distance. Latter simulation was confirmed by resolutions measurements. Placing the lenses outside the chamber also makes adjustments and additional modifications easier and cheaper. Complications arouse from the fact that the vacuum viewports could only be anti-reflection coated up to the size of DN40CF. Thus, we had to use custom-made zero-length reducers for the chamber's DN100CF flanges in order to keep the distance between the outside lenses and the ion trap short.

We followed a thorough cleaning and bake-out procedure of all vacuum parts to achieve a good UHV environment. Special care was taken to minimise the risk of contaminating the clean setup during assembly and installation of the trap. Only during the final revision of this thesis a proper set of AR-coated viewports was finally delivered by the company. We replaced the blind flanges with the viewports, closed the chamber and activated the strontium sources. Then another vacuum bakeout at $180\,^{\circ}$C was per-

formed and the NEG element of the NEXTorr D 100-5 vacuum pump was activated at a temperature of $80\,°$C. With this step the vacuum chamber is finally ready to trap ions. At the time writing this summary, the chamber is in the lab and has a vacuum pressure[1] below $2 \cdot 10^{-11}$ mbar.

The next step towards trapping ions will be to test the strontium sources. We will look for atomic fluorescence under illumination with the $461$ nm laser (the first step of the photoionisation) while heating the ovens to see if strontium is emitted. If the ovens work as intended, the only steps left over are to prepare the optical setup for shining laser light into the trap as well as connecting the RF source and the helical resonator for impedance matching. After these steps we will hopefully be able to quickly trap strontium ions and start working on Rydberg spectroscopy.

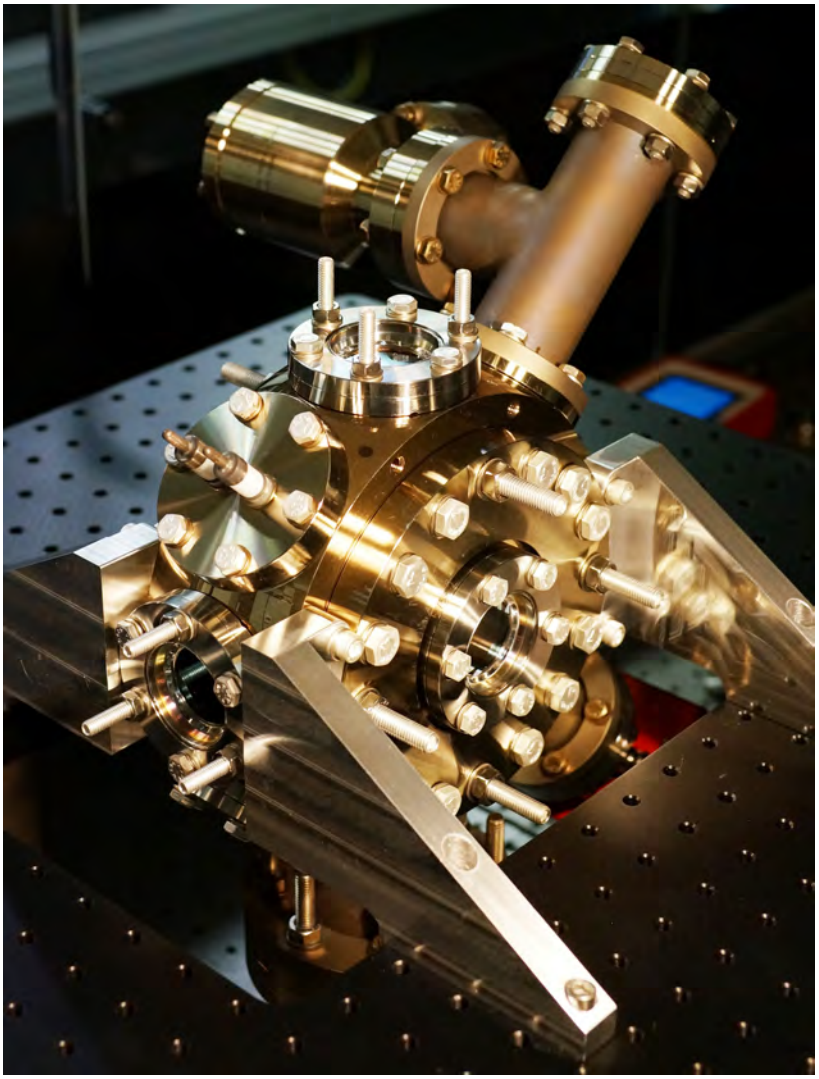

**Figure 5.1:** Vacuum chamber, finally closed with the AR-coated viewports at a pressure of $\leq 2 \cdot 10^{-11}$ mbar.

[1]This is the smallest pressure the ion pump can detect.

# Appendix A

# Macor oven holder

Oven holder, own design. Developed together with the mechanical workshop.

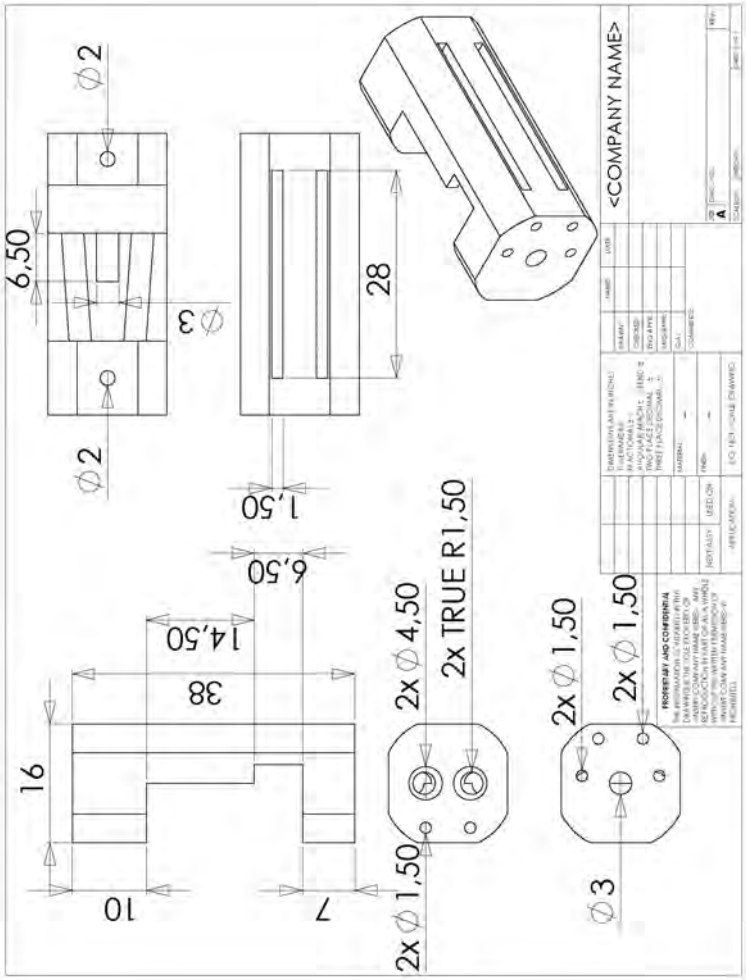

# Appendix B

# Custom zero-length reducer

Custom-made by VACOM.

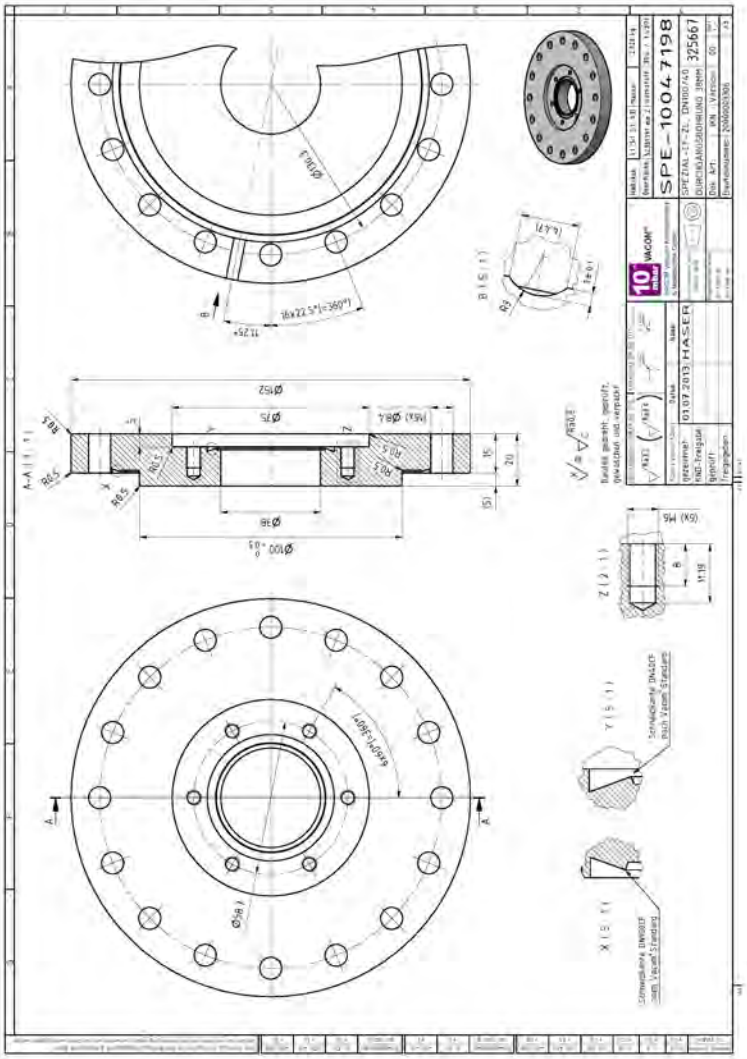

# Appendix C

# NEXTorr D 100-5 vacuum pump

The following graphs and specifications were supplied by Saes getters and were used to estimate the magnetic field of the NEXTorr D 100-5 vacuum pump at the center of the ion trap.

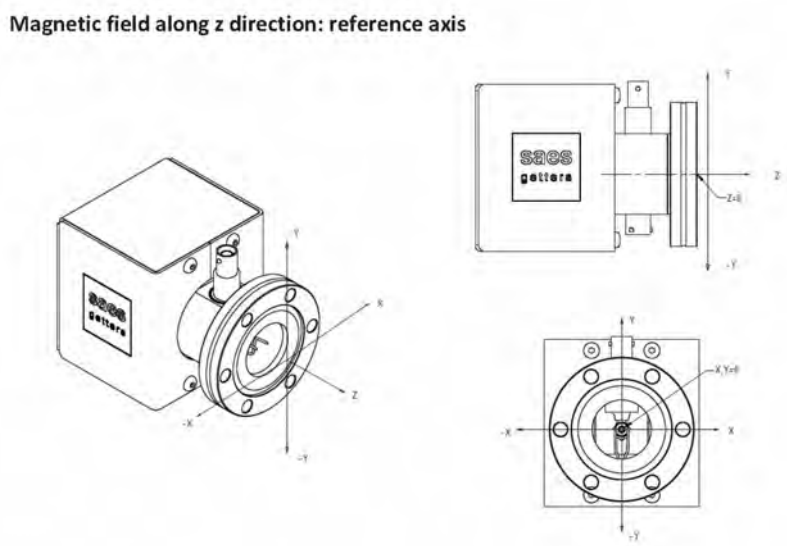


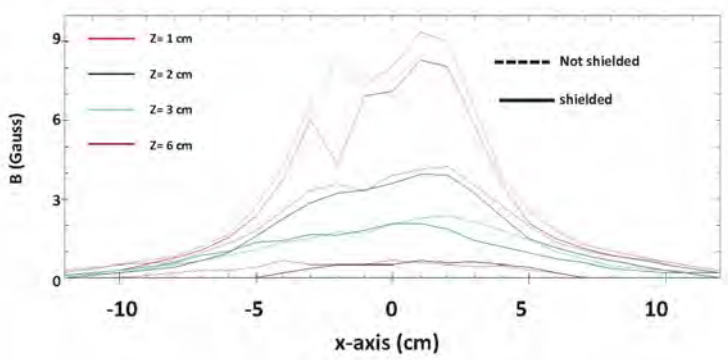

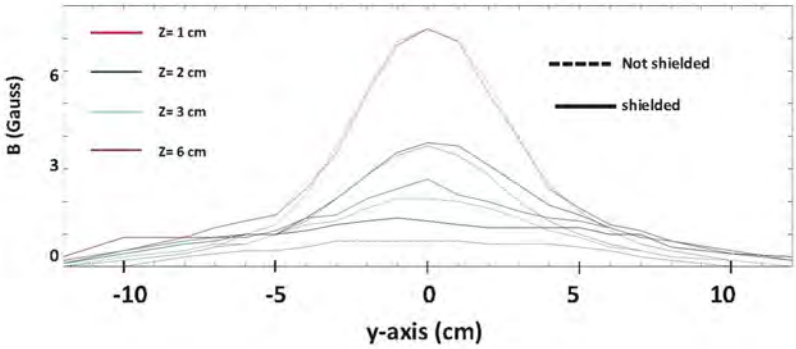


## Magnetic Field along X-Y plane: reference axis

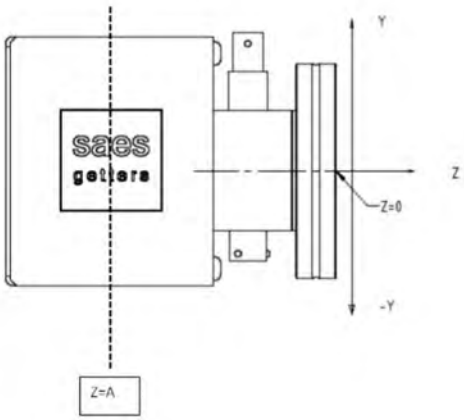


Not shielded

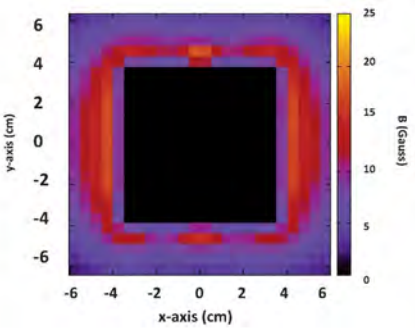


Shielded

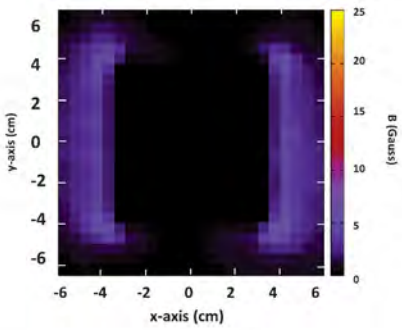


N.B.: the magnetic field characterizations along X-Y plane have been carried out at z=A position (see reference axis above)

# Bibliography


[1] R. P. Feynman, International Journal of Theoretical Physics **21**, 467 (1982), ISSN 0020-7748, URL http://dx.doi.org/10.1007/BF02650179.

[2] D. Deutsch, Proceedings of the Royal Society of London. Series A, Mathematical and Physical Sciences **400**, 97 (1985), ISSN 00804630, URL http://www.cs.princeton.edu/courses/archive/fall06/cos576/papers/deutsch85.pdf.

[3] P. W. Shor, in *Foundations of Computer Science, 1994 Proceedings., 35th Annual Symposium on* (IEEE, Los Alamitos, CA, USA, 1994), vol. 0, pp. 124–134, ISBN 0-8186-6580-7, URL http://dx.doi.org/10.1109/sfcs.1994.365700.

[4] J. I. Cirac and P. Zoller, Phys. Rev. Lett. **74**, 4091 (1995), URL http://link.aps.org/doi/10.1103/PhysRevLett.74.4091.

[5] C. Monroe, D. M. Meekhof, B. E. King, W. M. Itano, and D. J. Wineland, Phys. Rev. Lett. **75**, 4714 (1995), URL http://link.aps.org/doi/10.1103/PhysRevLett.75.4714.

[6] M. A. Nielsen and I. L. Chuang, *Quantum Computation and Quantum Information* (Cambridge University Press, Cambridge, England, 2012), ISBN 978-1-10700-217-3.

[7] H. Haffner, C. Roos, and R. Blatt, Physics Reports **469**, 155 (2008), URL http://arxiv.org/abs/0809.4368.

[8] R. Hughes and T. Heinrichs, *Arda quantum computing roadmap*, Army Research Office, USA (April 2004), URL http://qist.lanl.gov/qcomp_map.shtml.

[9] D. J. Wineland, Physica Scripta **2009**, 014007 (2009), URL http://stacks.iop.org/1402-4896/2009/i=T137/a=014007.

[10] D. P. DiVincenzo, Fortschr. Phys **48**, 2000 (2000), URL http://arxiv.org/abs/quant-ph/0002077v3.

[11] M. Müller, L.-M. Liang, and P. Lesanovsky, I. Zoller, New J. Phys. **10**, 093009 (2008), URL http://arxiv.org/abs/0709.2849.

[12] C. J. Foot, *Atomic Physics* (Oxford University Press, Oxford, England, 2010), ISBN 978-0-19-850696-6.

[13] F. G. Major, V. N. Gheorghe, and G. Werth, *Charged Particle Traps* (Springer, Berlin, 2005), ISBN 3-540-22043-7.

[14] G. Werth, V. N. Gheorghe, and F. G. Major, *Charged Particle Traps II* (Springer, Berlin, 2009), ISBN 978-3-540-92260-5.

[15] P. K. Ghosh, *Ion Traps* (Oxford University Press, Oxford, England, 1995), ISBN 0-19-853995-9.

[16] F. Rohde, Ph.D. thesis, Universitat Politècnica de Catalunya (2009), URL http://heart-c704.uibk.ac.at/publications/dissertation/rohde_diss.pdf.

[17] M. Brownnutt, Ph.D. thesis, Imperial College London, London (2007), URL http://heart-c704.uibk.ac.at/people/michael.brownnutt/BrownnuttThesis.pdf.

[18] A. Sørensen and K. Mølmer, Phys. Rev. Lett. **82**, 1971 (1999), URL http://link.aps.org/doi/10.1103/PhysRevLett.82.1971.

[19] D. J. W. D. Kielpinski, C. Monroe, *Architecture for a large-scale ion-trap quantum computer* (2002), URL http://www.nature.com/nature/journal/v417/n6890/full/nature00784.html.

[20] P. Schindler, D. Nigg, T. Monz, J. T. Barreiro, E. Martinez, S. X. Wang, S. Quint, M. F. Brandl, V. Nebendahl, C. F. Roos, et al., New Journal of Physics **15**, 123012 (2013), URL http://stacks.iop.org/1367-2630/15/i=12/a=123012.

[21] D. P. DiVincenzo, Phys. Rev. A **51**, 1015 (1995), URL http://link.aps.org/doi/10.1103/PhysRevA.51.1015.

[22] S. Ritter, C. Nölleke, C. Hahn, A. Reiserer, A. Neuzner, M. Uphoff, M. Mücke, E. Figueroa, J. Bochmann, and G. Rempe, Nature **484**, 195 (2012), URL http://dx.doi.org/10.1038/nature11023.

[23] T. F. Gallagher, *Rydberg Atoms* (Cambridge University Press, Cambridge, England, 1994), ISBN 0-521-38531-8.

[24] V. L. Lebedev and I. L. Beigman, *Physics of Highly Excited Atoms and Ions* (Springer, Berlin, 1998), ISBN 3-540-64234-X.

[25] F. Schmidt-Kaler, T. Feldker, D. Kolbe, J. Walz, M. Müller, P. Zoller, W. Li, and I. Lesanovsky, New Journal of Physics **13**, 075014 (2011), 1104.3102, URL http://arxiv.org/abs/1104.3102v1.

[26] W. Li and I. Lesanovsky, Applied Physics B **114**, 37 (2014), ISSN 0946-2171, URL http://dx.doi.org/10.1007/s00340-013-5709-6.

[27] D. Jaksch, J. I. Cirac, P. Zoller, S. L. Rolston, R. Côté, and M. D. Lukin, Phys. Rev. Lett. **85**, 2208 (2000), URL http://link.aps.org/doi/10.1103/PhysRevLett.85.2208.

[28] S. Gulde, D. Rotter, P. Barton, F. Schmidt-Kaler, R. Blatt, and W. Hogervorst, Applied Physics B **73**, 861 (2001), URL http://dx.doi.org/10.1007/s003400100749.

[29] M. Brownnutt, V. Letchumanan, G. Wilpers, R. Thompson, P. Gill, and A. Sinclair, Applied Physics B **87**, 411 (2007), ISSN 0946-2171, URL http://dx.doi.org/10.1007/s00340-007-2624-8.

[30] S. Removille, R. Dubessy, B. Dubost, Q. Glorieux, T. Coudreau, S. Guibal, J.-P. Likforman, and L. Guidoni, Journal of Physics B: Atomic, Molecular and Optical Physics **42**, 154014 (2009), URL http://stacks.iop.org/0953-4075/42/i=15/a=154014.

[31] C. Maier and F. Pokorny, *Digitale Laserstabilisierung am QuaSIRIO-Experiment*, Universität Innsbruck (2013).

[32] E. D. Black, American Journal of Physics **69**, 79 (2001), URL http://scitation.aip.org/content/aapt/journal/ajp/69/1/10.1119/1.1286663.

[33] C. Maier, *Laser system for the Rydberg excitation of Strontium ions*, Leopold Franzens University of Innsbruck (2013).

[34] R. D. Linde, *CRC Handbook of Chemistry and Physics (78th Edition)* (Crc Press Inc, 1997), ISBN 0-8493-0478-4.

[35] H. Haken and H. C. Wolf, *Atom- und Quantenphysik* (Springer-Verlag Berlin, Deutschland, 2004), ISBN 3-540-02621-5.

[36] J. D. Jackson, *Klassische Elektrodynamik* (Walter de Gruyter, Berlin, 2006), ISBN 3-11-018970-4.

[37] Alvatec, *Alvasources* (2013), URL http://www.alvatec.com/files/9013/3760/9166/alvasources-web-high.pdf.

[38] W. J. Smith, *Modern Optical Engineering* (McGraw-Hill Professional, 2000), ISBN 0-07-136360-2.

[39] K. M. Birnbaum, *Ultra-High Vacuum Chambers*, California Institute of Technology, Californa (2005), URL http://sourav-dutta.wikispaces.com/file/view/Ultra-High+Vacuum+Chambers.pdf.

[40] J. F. O'Hanlon, *A User's Guide to Vacuum Technology* (John Wiley and Sons, Inc., 2003), ISBN 0471270520.

[41] K. Jousten, *Thermal outgassing*, CERN (2000), URL http://cds.cern.ch/record/455558/files/open-2000-274.pdf.

[42] F. Rosebury, *Handbook of electron tube and vacuum techniques* (AIP, New York, 1993), ISBN 1-56396-121-0.

[43] A. Roth, *Vacuum sealing techniques* (American Institute of Physics, New York, 1994), ISBN 1-56396-259-4.

# Danksagung

Am Ende dieser Arbeit möchte ich die Gelegenheit ergreifen und mich bei denjenigen bedanken, die bei der Entstehung dieser Seiten und der ihnen zugrunde liegenden Arbeit im Labor direkt und/oder indirekt mitgewirkt haben.
Bedanken möchte ich mich an erster Stelle bei Markus Hennrich für die Möglichkeit, beim Aufbau dieses neuen Experiments von Anfang an dabei zu sein. Die Arbeit im Labor hat mir viele wertvolle und interessante Einblicke und Erfahrungen ermöglicht. Speziell möchte ich mich auch für die Betreuung im Labor sowie beim Verfassen dieser Arbeit bedanken. Hier hast du echt viel Zeit investiert!
Weiters möchte ich mich bei Christine Maier, Gerard Higgins und Johannes Haag für die gemeinsame Zeit im Labor bedanken. Die Zusammenarbeit mit euch (teilweise schon seit längerem durch etliche Praktika erprobt und getestet) war und ist mir ein Vergnügen - auf dass es so weitergehe! Gerard gebührt noch ein extra „Danke Schön“ für das Korrekturlesen dieser Arbeit. Ebenfalls namentlich erwähnen möchte ich Michael Guggemos und Daniel Heinrich für die Beantwortung vieler Fragen zum Aufbau der Falle und der Kammer. Zu guter Letzt möchte ich mich auch noch bei den restlichen Mitgliedern der Arbeitsgruppe um Rainer Blatt für das angenehme und konstruktive Arbeitsklima bedanken sowie Christine, Kirsten und Philip, die mit mir das Büro teilen beziehungsweise geteilt haben.

Ein eigener Abschnitt gebührt jenen Mitstudenten und sonstigen Weggefährten, die mir in den Jahren in Innsbruck zu guten Freunden geworden sind. Ob bei der gemeinsamen Vorbereitung auf Prüfungen, dem Abarbeiten von ungezählten Übungszetteln oder sonstigen (eventuell auch mal gar nicht studienrelevanten) Aktivitäten, ich hab die Zeit mit euch sehr genossen. Für die Zukunft wünsche ich euch alles Gute!

Abschließend möchte ich mich an jene wenden, die mir dieses Studium ermöglicht haben: meiner Familie, allen voran meinen Eltern. Ich danke euch für die eure Unterstützung, sei es in finanzieller oder sonstiger Hinsicht - ohne euch wäre dieses Unterfangen wohl nicht möglich gewesen!

**Eidesstattliche Erklärung**

Ich erkläre hiermit an Eides statt durch meine eigenhändige Unterschrift, dass ich die vorliegende Arbeit selbständig verfasst und keine anderen als die angegebenen Quellen und Hilfsmittel verwendet habe. Alle Stellen, die wörtlich oder inhaltlich den angegebenen Quellen entnommen wurden, sind als solche kenntlich gemacht.

Die vorliegende Arbeit wurde bisher in gleicher oder ähnlicher Form noch nicht als Magister-/Master-/Diplomarbeit/Dissertation eingereicht.

| | |
|---|---|
| Datum | Unterschrift |